Feasibility of using wet abrasive jet machining to produce flat and crack-free micro-textures on reaction bonded silicon carbide

Yan Hu *

College of Mechanical and Electrical Engineering, Nanjing University of Aeronautics & Astronautics, Nanjing, 210016, PR China

ARTICLE INFO

ABSTRACT

Reaction-bonded silicon carbide (RB-SiC) is a composite ceramic that comprises of hard SiC grains and brittle Si matrix. Surface texture with well machining qualities, in particular, is difficult to be fabricated on RB-SiC in conventional machining conditions since the removal of material inevitably induces some unexpected surface defects. In this paper, the feasibility of using a wet abrasive jet machining process (wet AJM) to produce smooth and crack-free micro-features on RB-SiC was investigated. Three commercial abrasives were employed to test the machining responses. The hardness of abrasive was found to be critical and dominate the machinability of RB-SiC. The hardest synthetic diamond (SD) abrasive could crush the SiC grains, thereby providing the highest machining efficiency and a relatively smooth face. The relatively soft abrasives, including aluminum oxide (Al_2O_3) and green SiC, tend to break or rebound during the impact. After removing the Si matrix, SiC grains would be exposed and be to some degree protective of the target; therefore, the machined texture was shallow and rough. Since the particles in the lateral flow rolled freely, there were no obvious cracks on the inner surface of the machined texture compared to the machining without water. The variation of the machining profile had an inherent correlation to the mask thickness, nozzle motion speed and particle size. With these optimized parameters, it is feasible to use the wet AJM to fabricate complex micro-structural arrays on RB-SiC with good precision and surface quality.

1. Introduction

Reaction-bonded silicon carbide (RB-SiC) ceramic is a composite material, offering improved wear-resistance due to its microstructure that tough silicon carbide (SiC) reinforcements are surrounded by the infiltration of molten silicon (Si). As reported by Chen et al. (2012), RB-SiC exhibits the properties of 100 % dense, high stiffness, high chemical inertness, light weight and low cost, which makes it one of the attractive candidate materials for mechanical seals. Surface-textured mechanical seals involve fabricating micro-holes, channels, repeated waves, etc., on the contact faces, having been proven to ameliorate the service life. To ensure some effects such as generation of fluid dynamic pressure and storage of lubricant, the texture unit must be shallow, usually ranging from 5 μm to 100 μm in depth and 50 μm to millimeters in width, as noted by Melentiev and Fang, 2020. In addition, surface within the textures needs to be sufficiently smooth and uniform to allow the lubricant to flow.

Researchers must determine how to efficiently introduce desired micro-patterns on ceramic surfaces. However, due to the hard and brittle natures of SiC grains, fabricating such surface textures on RB-SiC is difficult. This has been confirmed by the literature of Patten et al. (2005) on diamond cutting of single-crystal SiC. Only under the parameters of low feed speed and critical depth of cutting (DOC) less than 38 nm, ductile mode cutting can be achieved. These operating parameters selected to avoid crack initiation inevitably cause low removal rate and long machining time. A greater difficulty may arise from the non-uniform structure, i.e., the SiC grains embedded in the softer Si matrix. The uneven removal of each component within RB-SiC results in a worse surface finish, as reported in the work of Yamamura et al. (2012).

It is important to choose the machining methods according to the specific application and material. Unfortunately, contact machining methods, such as ordinary cutting, ultra-precision diamond micro-cutting and micro-grinding, will alternatively plow the matrix (Si) and reinforcement (SiC), and then experience different plowing loads for different phases, thus causing severe vibration, tool wear and surface damages such as fractured SiC surface, intercrystalline cracks, pores and micro-pits, as noted by Zhang et al. (2019). Zhang et al. (2015) indicated
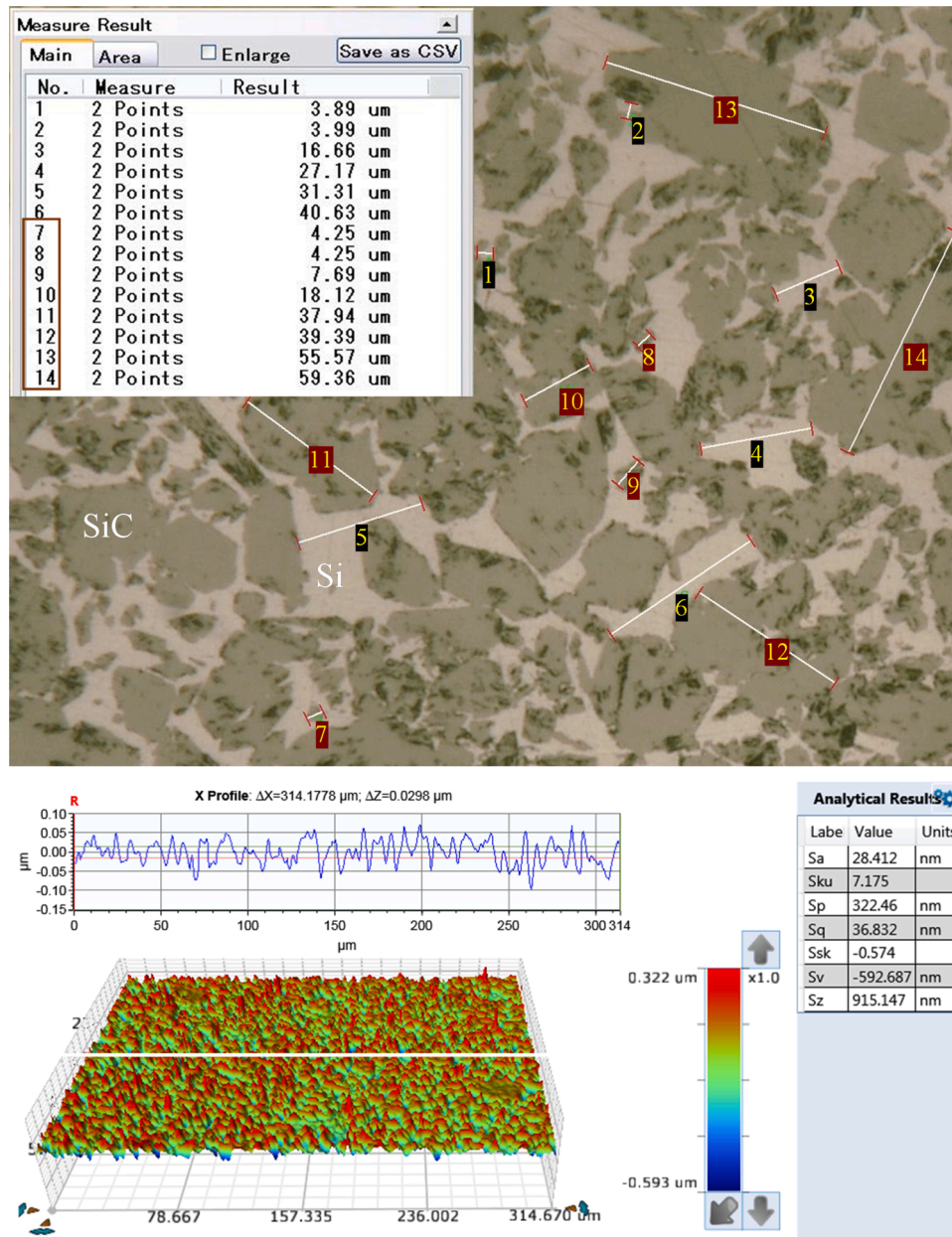

Fig. 1. Microstructure of the polished RB-SiC (nos. 1–6 are the size of Si matrix and nos. 7–14 are the size of SiC grains).

that micro-pits at the phase boundary are inevitable because of the material micro-structure and its interaction with abrasive grits, even if the feed rate drops to a very low value, 0.1 mm/min. Also, the instantaneous temperature during grinding may cause the oxidation for both SiC and Si cluster. Other methods such as electric discharge machining (EDM), electrochemical machining and laser machining are also not suitable for RB-SiC due to the high content of reinforcement, the presence of heat-sensitive Si matrix and the low conductivity of material. In these thermal, chemical or thermochemical methods, some machining defects inevitably induce, including thick oxide layer (viz. SiO_2) in the work of Shen et al. (2015), SiC decomposed into Si and C in the work of Ishikawa et al. (2014), phase transformation in the work of Clijsters et al. (2010), recast layer, melt slag, heat-affected zone and micro-crack region in the work of Rao et al. (2020). As shown in the observation of Yamamura et al. (2012), expensive methods, such as atmospheric pressure plasma, plasma with the process gas of helium based water vapour and reactive ion etching (RIE), are often difficult to select parameters to reduce the different corrosion rate between the SiC and Si.

Abrasive jet machining (AJM), as a cold and non-contact process, is well-suitable for micro-machining of hard and brittle materials like glass and ceramics (Saragih and Ko, 2009a). Saragih and Ko (2009b) indicated that AJM is attractive because of its high material removal rate on brittle materials, high flexibility, low capital and operating costs, and negligible thermal effect when compared to other machining methods. One of the typical applications of AJM process is decorating or texturing ductile or brittle materials, as typically reviewed by Belloy et al. (2002) and Park et al. (2005). However, relevant existing literature on AJM of RB-SiC was limited to the erosion test by Huang et al. (2001) and hole drilling by Nguyen et al. (2018). To the knowledge of the authors, there have been no attempts to utilize the AJM to fabricate rectangular texture on RB-SiC. The feasibility of using AJM to create desired micro-patterns on this two-phase material was still unknown and deserves further investigation. In addition, the quality of the surface eroded by AJM in the past reports is poor. For example, when using the dry abrasive-air jet process (dry AJM, 0.1−0.6 MPa), micro-cracks were easily formed on the matrix surface and at the grain boundary, as noted by Huang et al.

Table 1
Physical properties of the workpiece material and the employed abrasives.

Material	Abrasive			Workpiece
	Al_2O_3	Green SiC	SD	RB-SiC
Micro hardness (GPa)	22.12	28.53	98	13.12 (Si), 24.53 (SiC)
Mohs hardness	8–9	9.5	10	6.5 (Si), 9.2–9.3 (SiC)
Knoop hardness (HK)	2100	2480	7000	
Hardness (HV)	1800	2500	8000	
Toughness (MPa*m$^{1/2}$)	3–3.5	3.5–4.5	7–11	3–4
Density ($\times 10^3$ kg. m^{-3})	3.97	3.21	3.52	3.02–3.05
Shape	Irregular	Irregular	Blocky	Rotor ring
Volume fraction				SiC (90 vot%), Si (10 vot%)
Apparent porosity				< 0.1 %

(2001). The report conducted by Nguyen et al. (2018) who used abrasive slurry jet (ASJM, 20−25 MPa) process to machine RB-SiC indicated that the slurry flow can avoid the formation of crack. Notwithstanding, due to the wavy viscous flow developed by the high-pressure slurry jet impact, wavy pattern was formed around the hole. Additionally, surface roughness measured at the bottom was up to 25.79 μm.

In summary, as a typical hard-to-machine material, RB-SiC ceramic machining faces lots of difficulties. Although large-scale fracture-free surfaces and even mirror finishes have been achieved on RB-SiC via the disk polishing and ultra-precision micro-grinding processes, these methods are either of low efficiency or lack the flexibility to fabricate complex surface textures. For RB-SiC with high reinforcement content, electronic-grade surface within textures is nearly impossible to achieve

by conventional machining processes. Most of the recently developed techniques for micromachining of RB-SiC, including the jet machining mentioned above, inevitably introduce additional machining defects. Among them, high roughness and microscopic cracks are the most common, which are not allowed to appear in the sealing equipment that works under harsh conditions such as high speed and high temperature. There may be a pressing need to discover a reliable and no-additional-damage method to fabricate microfeatures with smooth and high-integrity surface on RB-SiC.

Here this research attempts to solve the technical challenge of surface damages in conventional machining of RB-SiC by introducing a low-pressure (air pressure of 0–0.6 MPa) wet AJM micromachining process for high-quality and damage-free surface. The feasibility of using the wet AJM process to fabricate microfeatures on RB-SiC surface was investigated. The machinability was tested by wet AJM containing different abrasives. An increased machining efficiency and a reduced surface roughness could be achieved via the selected SD abrasive. Related particle erosion mechanisms when subjected to the action of abrasives were presented in detail. In the wet AJM, a typical difference from the conventional abrasive-air jet (dry AJM) is that the airflow not only carries abrasive particles, but also water. With the water used, a smooth surface without obvious surface cracks could be generated on RB-SiC. The role of water in obtaining the crack-free surface was discussed. Based on the selected SD abrasive, the wet AJM process was further optimized to fabricate textures with a more precise machining profile; and, finally, the application of surface texturing was used to demonstrate the capability of the wet AJM on RB-SiC. Overall, the novelty of this paper is that it introduces a relatively inexpensive method to produce structured engineering surfaces on RB-SiC that have a relatively high surface quality compared with other micro-machining methods.
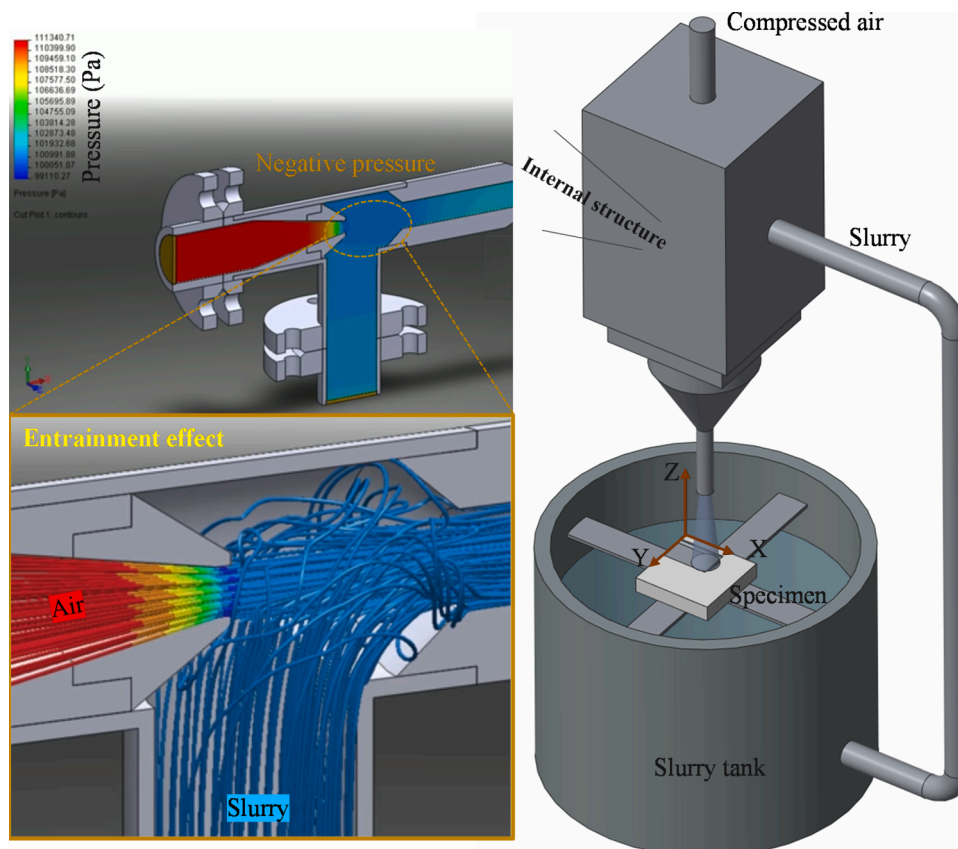
Fig. 2. Schematic description of wet abrasive jet machining equipment (not to scale).
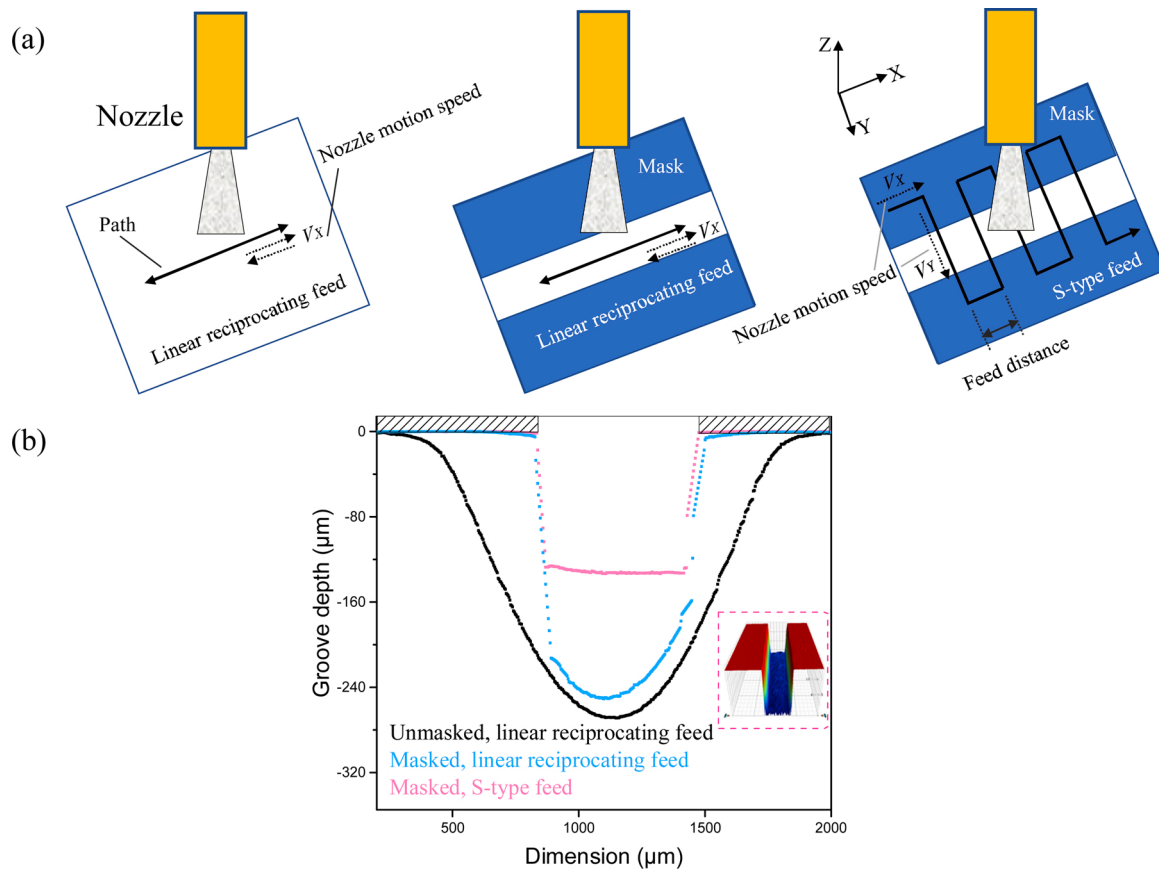
Fig. 3. (a) Three types of nozzle motion path; (b) typical texture profiles machined on RB-SiC by using wet AJM with the three paths.

2. Experimental procedure

2.1. Characterization of RB-SiC

The RB-SiC workpiece is provided by Yuanda Mechanical Seal Co., Ltd, China. Fig. 1 shows its microstructure under the optical microscope. It is a two-phase dense composite that comprises of 90 vot% SiC, 10 vot% Si and grain/phase boundary, in which fine SiC grains are surrounded by the penetration of molten Si. The size of SiC grains and Si matrix varies greatly, ranging from 4 µm to 60 µm. The surface roughness (S_a) after fine grinding is 28.412 nm. No obvious pores exist in the material. According to the research of Zhang et al. (2015), the black points on the SiC grains are micro-fractures and micro-pits induced during the grinding process. The detailed physical properties of RB-SiC are listed in Table 1.

2.2. Wet AJM setup

Abrasive air-jet machining (dry AJM) is a dry machining process that uses an air jet with entrained particles to mechanically etch the target surface. Here, to well machine the RB-SiC, a wet abrasive air-jet machining (wet AJM) technology was developed whereby a method that uses compressed air to accelerate the premixed slurry (mixture of micro-abrasives and water) through a small nozzle to remove material from the substrate. The schematic diagram of wet AJM is shown in Fig. 2.

As seen in Fig. 2, to realize the sustainable supply of premixed slurry, a special nozzle was designed with an air motive tube (0.7 mm in diameter), a mixing chamber and a relatively small focus tube (1.9 mm in diameter). When compressed air passes through the air motive tube at a high speed, a region of low pressure is generated in the mixing chamber. This low-pressure region draws the slurry into the nozzle.

Then, the erodent and carrier water are mixed with the airflow to form a slurry jet through the focus tube. Wakuda et al. (2002) indicated that the precious abrasive, synthetic diamond (SD), is usually uneconomical in AJM process where dry particles are not available for recycling. The abrasive consumption is large, and fine particles are easy to float in the air, thus causing dust pollution. The wet AJM used here can eliminate these dilemmas by dissolving a small amount of abrasive particles in the water. The ejective slurry can flow into the slurry tank and then be sucked into the nozzle again. The slurry in the tank was constantly stirred by magnetic rotor during use to keep homogeneous. Due to the short-time processing and the small-scale removal of materials, the reuse of abrasives has little effect on the machining result. Jet velocity can be adjusted by changing the operating pressure. According to the research by Iwai et al. (2009), the velocities of wet AJM at 0.6 MPa are estimated to be slightly higher than 110 m/s.

2.3. Machining details

All experiments were conducted using the wet AJM operating system. During the experiments, a nozzle-to-workpiece height (standoff distance) of 10 mm and a slurry concentration of 10 wt% were considered because of their relatively high machining efficiencies. Obliquity of the jet relative to the target was shown to be a significant factor. Angles other than 90 ° results in varying levels of under-etching of the sidewalls, thus a jet impact angle of 90 ° was chosen. The machined textures were measured using a digital microscope (Keyence, Japan) with a step size of 2 µm along the two planar scanning directions. The display resolution of microscope was 0.1 µm. Roughness (S_a, R_a, and S_z) and surface topography were observed and analyzed using the 3D optical profilometer (Bruker, USA). The vertical resolution of optical profilometer was less than 0.1 nm. The surface roughness (S_a) was measured on a rectangle region of 300 µm × 100 µm at the bottom of the machined

Table 2
Particle size distribution for the employed abrasives.

Size range (μm)	3–5	5–7	7–9	9–11	11–14	14−17
Al$_2$O$_3$ (6.5 μm)	10 %	82 %	8 %	0 %	0 %	0 %
Al$_2$O$_3$ (13 μm)	0 %	0 %	0 %	2 %	94 %	4 %
SiC (6.5 μm)	5 %	85 %	10 %	0 %	0 %	0 %
SiC (13 μm)	0 %	0 %	0 %	3 %	90 %	7 %
SD (6.5 μm)	3 %	92 %	5 %	0 %	0 %	0 %
SD (8 μm)	0 %	3 %	94 %	3 %	0 %	0 %
SD (10 μm)	0 %	0 %	3 %	93 %	3 %	1 %
SD (13 μm)	0 %	0 %	0 %	5 %	88 %	7 %

texture. All instruments were calibrated before use to ensure the accuracy of measurements.

In jet machining, the features formed on the workpiece, including its dimension, internal shape, surface roughness, etc., are caused by the erosion of a large number of particles. Noted that not all of abrasive particles in the jet are uniformly distributed and have the same impact energy to form a uniform erosion depth, thus it needs to illustrate the method of obtaining a rectangular machining profile. According to the research of Ghobeity et al. (2009), flat areas and transitional slopes on glass could be obtained by oscillating the nozzle relative to the target in a direction perpendicular to the groove direction. In the oscillation, nozzle was driven to move in a S-type path across the unmasked area, as shown in Fig. 3(a). In the S-type path, nozzle first moved along the *X* direction by a feed distance, and then moved along the *Y* direction by a distance larger than the width of the mask opening. In addition, other two moving methods were also conducted to test the jet erosion profile, including the linear reciprocating feed mode with or without mask. SUS304 was selected as the mask material in this study because of its good erosion resistance and machining properties. The mask with a thickness of 0.2 mm and an opening width of 500 μm was fabricated by laser machining. Synthetic diamond (SD) abrasive with an average equivalent circular diameter of 13 μm was used, and its size distribution is shown in Table 2. In the linear reciprocating feed mode, nozzle motion speed (V_X) is 0.3 mm/s. In the S-type feed mode, nozzle motion speed (V_X) is 1 mm/s, nozzle motion speed (V_Y) is 0.3 mm/s, and feed distance is 50 μm. Fig. 3(b) presents the machined results when using the three feed modes. The results show that when mask and S-type feed mode were employed, the machined texture was characterized by a

rectangular outline with a uniform erosion depth and relatively steep sidewalls. Herein, the S-type feed mode and mask were used to obtain a rectangular machining profile.

Aiming at optimizing the wet AJM process to fabricate microfeatures with smooth and high-integrity bottom surface on RB-SiC, the content of the present paper was designed into the following two parts. First, based on the use of mask and S-type feed mode, different types of abrasives were used to reduce the difference in removal rate of Si and SiC phases with the aim of obtaining a flat-bottomed texture. Then, the mask thickness, nozzle motion speed and particle size were further optimized to generate a more accurate contour. Single factor experiments were used in this paper.

3. Results and discussion

3.1. Method of obtaining a relatively smooth-faced texture
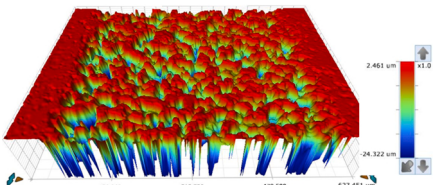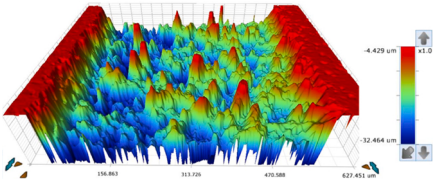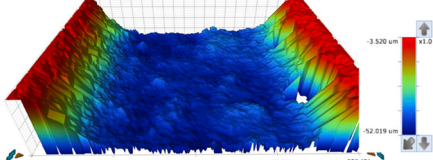
3.1.1. Machining response of using different abrasives

Due to the presence of soft Si phase and hard SiC phase, it is necessary to select the abrasive with a suitable hardness to test the machining response. Three kinds of abrasives, having a typical angular shape and the same average equivalent circular diameter, were employed to evaluate the machinability of material, including the aluminum oxide (Al$_2$O$_3$) abrasive, green SiC abrasive and synthetic diamond (SD) abrasive. Their properties and ranges of diameter are shown in Table 1 and Table 2, respectively. The hardness of Al$_2$O$_3$ abrasive is lower than that of SiC phase, the hardness of green SiC abrasive is equivalent to that of SiC phase, and the hardness of SD abrasive is higher than that of SiC phase. The hardness of all abrasives is higher than that of Si phase. Under the conditions of air pressure of 0.3 MPa, particle size of 6.5 μm, metal mask and S-type feed mode with nozzle motion speed (V_X) of 1 mm/s, nozzle motion speed (V_Y) of 0.3 mm/s and feed distance of 50 μm, the machined results can be found in Table 3 and Fig. 4(a).

From Table 3, it can be found that the removed volume and roughness caused by Al$_2$O$_3$, SiC and SD abrasive particles are quite different. The texture machined by Al$_2$O$_3$ abrasive is almost in an unprocessed state. There are many protuberances that are as high as the raw surface. The average machining depth is only 2.362 μm. The maximum value between the peak and valley is 26.783 μm, and the average surface roughness at the bottom is 0.358 μm. In the case of using SiC abrasive,

Table 3
Textures machined by wet AJM with various abrasives.

Abrasive type	3D surface topography of the machined texture	h, μm	S_a, μm	S_z, μm
Al$_2$O$_3$ (aluminum oxide)		2.362	0.358	26.783
SiC (green silicon carbide)		11.325	2.676	28.035
SD (synthetic diamond)		49.436	0.626	3.252

Note: *h*–average machining depth; S_a–surface roughness; S_z–maximum value between the peak and valley.

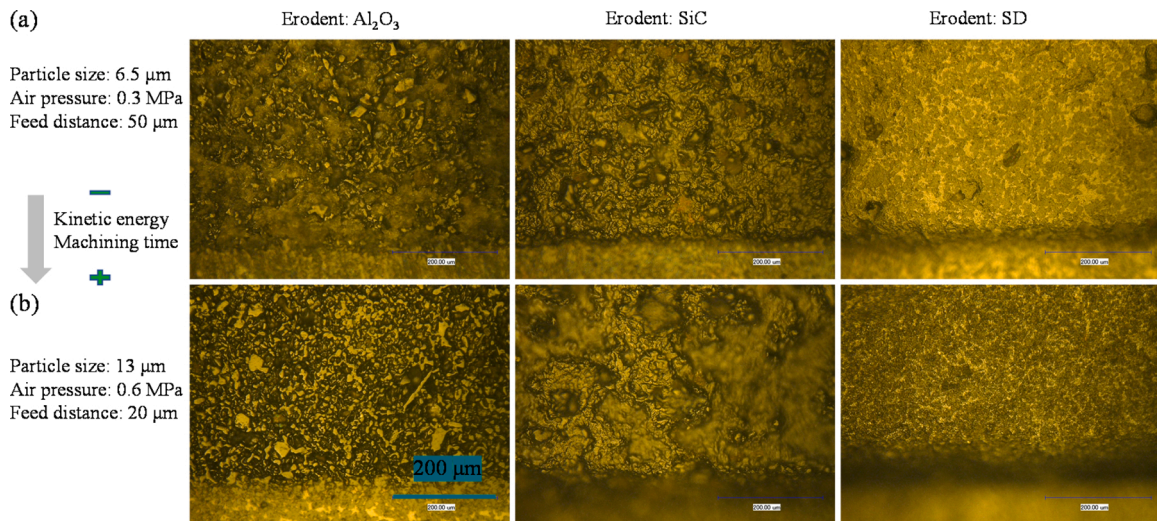**Fig. 4.** Optical surface topologies of the textures processed with the Al$_2$O$_3$, SiC and SD abrasives at the different processing parameters.

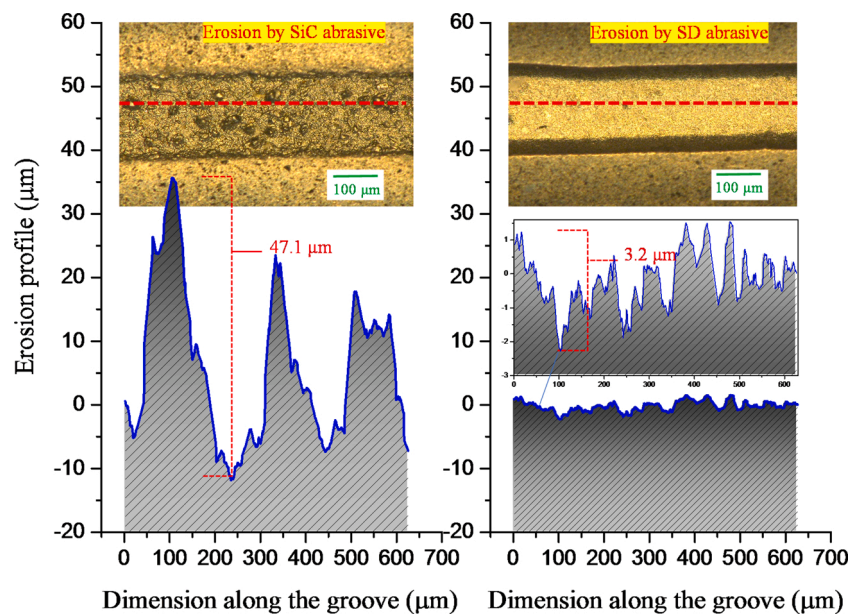**Fig. 5.** Comparison of surfaces eroded by SiC and SD abrasive particles at particle size of 13 μm, air pressure of 0.6 MPa and feed distance of 20 μm. The dashed lines are the measuring positions.

although the average depth is 11.325 μm, there are still numerous micro-protuberances on the newborn surface, and the average roughness is as high as 2.676 μm. Interestingly, on the erosive surface by SD abrasive, the micro-bulges are obviously removed, and the texture has a deep and flat bottom. The average depth is 49.436 μm, and the average bottom surface roughness is only 0.626 μm. It can be found that the machining efficiency and quality largely depends on the employed abrasives. Within the same time, machining efficiency of SD is 20.93 and 4.37 times that of Al$_2$O$_3$ and SiC, respectively. The machining quality is the best for SD abrasive impact compared with the other particles.

For a comparison with Fig. 4(a), Fig. 4(b) shows the optical surface topologies of the textures processed with the Al$_2$O$_3$, SiC and SD abrasives, but at larger particle size of 13 μm, higher pressure of 0.6 MPa and smaller feed distance of 20 μm. The increase in air pressure and particle size is essentially an increase in impact energy; the decrease in feed distance is essentially an increase in machining time. The average machining depth was 5.547 μm, 42.254 μm and 155.512 μm, respectively. Surface roughness measured at the bottom of the textures was

0.382 μm, 3.382 μm and 0.732 μm, respectively. The results (Fig. 4) show that the change of processing parameters greatly alters the volume of material removed, which is the same as the performance measures in abrasive water jet machining (AWJM) of TiB$_2$ particles reinforced Al7075 composite where the water pressure, transverse speed and standoff distance were changed (Manoj et al., 2018). However, it appears that the roughness obtained is not influenced significantly by the further increase of air pressure, particle size and machining time. The hardness of the abrasive particle was therefore found to have a controlling effect on the surface roughness during the wet AJM of RB-SiC.

Wakuda et al. (2002) indicated that when Al$_2$O$_3$ abrasive was applied for the dry AJM of alumina ceramics, only slight coarsening occurred on the surface and there is no engraving. The reason is that the softest abrasive, aluminum oxide (Al$_2$O$_3$), is not hard enough to cause erosion. When Al$_2$O$_3$ abrasive was employed in the wet AJM, the same erosion performance could be found in the machining of RB-SiC. Only a small amount of the soft Si matrix was removed, and the remained SiC grains were as high as the raw surface (see Table 3). Wakuda et al.
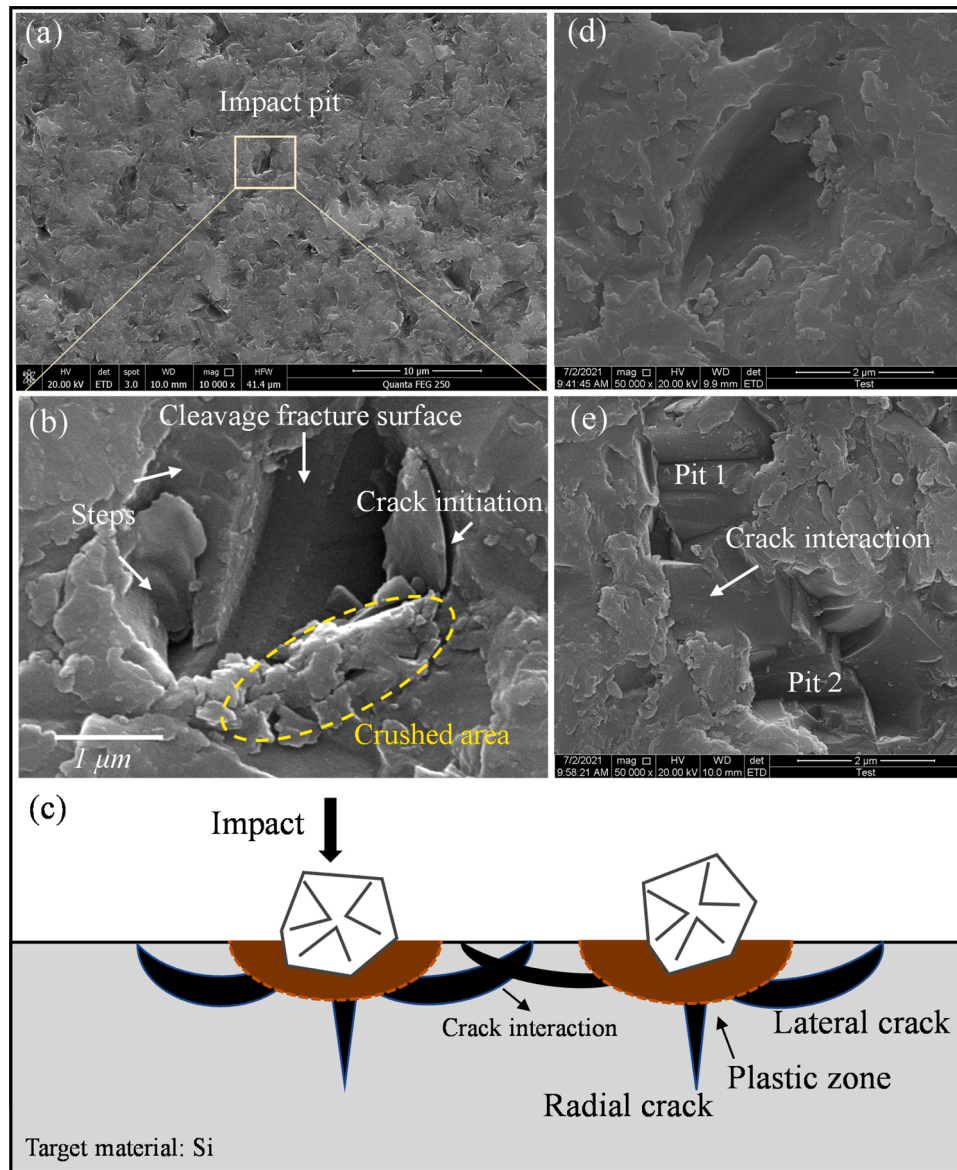
Fig. 6. (a) SEM image of Si surface eroded by SiC abrasive and (b) enlarged rectangle in (a); (c) the related erosion mechanism; (d) surface eroded by Al$_2$O$_3$ abrasive; (e) surface eroded by SD abrasive.

(2003) also indicated that in the AJM of alumina ceramics, SD abrasive easily caused a high machining efficiency and a rough appearance, whereas SiC abrasive produced a smooth surface. Conversely, the results in Fig. 5 show that the erosion of RB-SiC are significantly different from the above mentioned erosion of alumina ceramics. That is, SD abrasive can easily lead to a smooth and flat surface, whereas SiC abrasive tends to cause a rough surface. For the surface eroded by SiC abrasive, the maximum value between the peak and valley is up to 47.1 μm; while for the surface eroded by SD abrasive, the maximum value is as low as 3.2 μm. The reason for this difference may be related to the complex microstructure of RB-SiC. In the study conducted by Wakuda et al. (2003), the target is the alumina ceramics that can be regarded as a single-phase material, because the composition of alumina is up to 98 %, which is different from the two-phase material, RB-SiC. Therefore, it should reveal the erosion characteristics and mechanisms through the analyses on its microstructure, as will be discussed in detail in the next section.

3.1.2. Material removal mechanism

After confirming the possibility of obtaining a rectangular texture with a low-roughness surface, it is necessary to investigate whether cracks occur in the machining process by observing the erosive surface. The occurrence of cracks is related to the brittle erosion mechanism. When discussing the material removal mechanism of RB-SiC, due to the presence of pure Si phase in the material, it is first necessary to clarify the erosion mechanism of neat Si wafer. Under the conditions of metal mask (0.2 mm in thickness, 500 μm in width), S-type feed mode, nozzle motion speed (V_X) of 1 mm/s, nozzle motion speed (V_Y) of 0.3 mm/s, feed distance of 20 μm, air pressure of 0.6 MPa and 13-μm average size, wet AJM erosion of neat Si wafer was investigated. Fig. 6 shows the SEM images of Si surface eroded by SiC abrasive. As seen in Fig. 6(a), many conchoidal fractures can be found on the surface eroded by SiC abrasive, which is a typical brittle erosion mechanism. For a better presentation, a megascopic conchoidal fracture is shown in Fig. 6(b), consisting of a highly crushed area and a shell-like structure containing cleavage fracture surfaces and steps. Fig. 6(c) shows the related erosion process. When particles hit the Si surface, a plastic zone is formed below the impact zone. The tensile stress is induced to create a system of microcracks. Particles with sufficient impact energy further promote radial cracks to penetrate the substrate, thereby reducing the strength of the
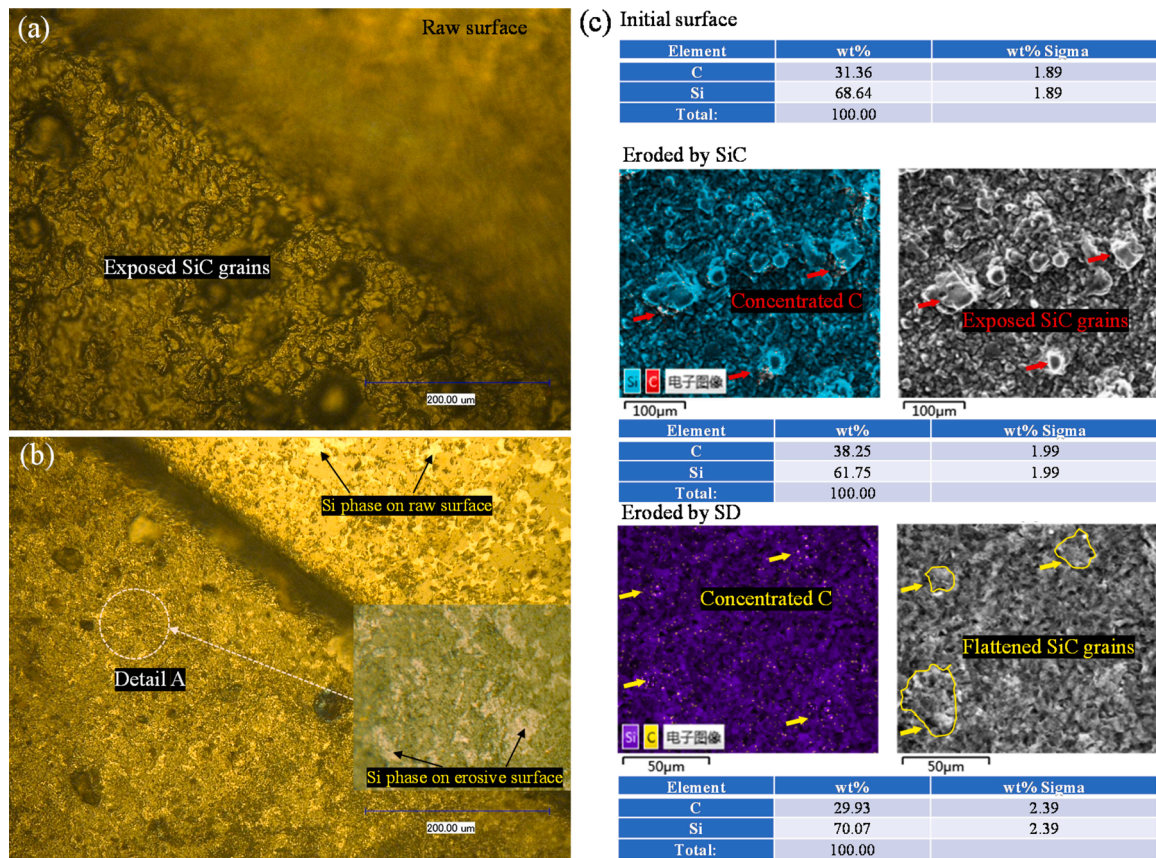
Fig. 7. Optical surfaces of RB-SiC eroded by (a) SiC abrasive and (b) SD abrasive; (c) the related EDS microscopic chemical analyses.

material. The lateral cracks parallel to the surface will interact and expand with other cracks, eventually forming numerous shell-shaped fractures. According to the analysis of erosion sites, it can be concluded that the removal of the Si material is mainly achieved by the formation of minor chipping. Similar marks for forming chipping were observed on the surfaces impacted by Al_2O_3 and SD abrasives, as shown in Fig. 6(d) and (e).

Fig. 7 shows the morphology and EDS microscopic chemical analysis of RB-SiC surface eroded by SiC and SD abrasive. As shown in Fig. 7(a), many black bulges can be found on the erosive surface of SiC abrasive. From Fig. 7(c), the carbon element is relatively concentrated on the surface of the bulges, indicating that these black bulges are the SiC phase. It can be inferred that on the erosive surface of SiC abrasive, the Si phase is completely removed, and then a large amount of SiC grains are exposed. Due to the removal of Si phase, the mass fraction of carbon increases from 31.36 %–38.25 % (see Fig. 7(c)). While as shown in Fig. 7 (b), there are almos t no raised SiC grains on the surface eroded by SD abrasive. Many embedded Si phases (light area in enlarged view of detail A) can be seen around the black SiC grains. In this case, the mass fraction of carbon dose not change much (31.36 % vs 29.93 %). To investigate the erosion mechanism of RB-SiC, a single exposed SiC grain and a local surface eroded by SD abrasive are enlarged in Fig. 8. The machining conditions are the same as those of Si.

Fig. 8(a) implies that the SiC abrasive, particularly in this low air pressure of 0.6 MPa, cannot pierce into the tough SiC grains to initiate cracks. During the impacts, a considerable part of the SiC particles will rebound or fracture. Many localized impact pits can be found on the erosive surface of SiC grains. According to the research of Nouraei et al. (2013), the plastically deformed craters are a performance of ductile erosion behavior. It is believed that when the erodent hardness is equal to or less than the hardness of the target, the kinetic energy of impacting particles tends to be consumed, not by material removal, but by

deformation or fracture of the impact abrasives themselves. Of course, some SiC particles acting on the tough SiC surfaces tend to move towards the adjacent material, Si matrix. Then, the Si matrix can be contacted by the wedging action of abrasives. In the gap of two SiC grains, rolling of the contact abrasive promotes the shear stress and then erodes the Si matrix. On the erosive surface of Si matrix (phase), many cleavage fractures are found (see Fig. 8(a)). This erosion morphology is consistent with that on the pure Si wafer shown in Fig. 6, indicating that the erosion of Si matrix is a brittle mode. According to these erosion marks, it is thought that the RB-SiC surface to the impact by SiC abrasive was subjected to a combination of both ductile and brittle erosion mechanism. Fig. 8(b) shows the local surface machined under the same conditions as the SiC abrasive, but using a harder SD abrasive. Compared with the surface eroded by SiC abrasive, the whole surface presents a relatively flat-fracture morphology. Obviously, any protruding SiC grains has been removed. As seen in Table 1, the hardness and toughness of SD abrasive is far greater than that of SiC grains, thus giving the erodent particles a greater ability to penetrate into the target without suffering plastic deformation, fracturing, disintegration or rounding-off themselves. Differing from the response by the SiC abrasive impact, most of the impact energy of SD abrasive is apportioned to the fragmentation of SiC grains due to its extremely high hardness. It can be verified by observing its SEM morphology. As shown in Figs. 7(c) and 8 (b), the surfaces of the erosive SiC grains are always approximately flush to the surface of the Si matrix. This implies that the hardness of SD is high enough to completely crush anyexposed grains, while the remaining part is still on thesub-strate. Of course, the grains are not completely flattened. The average height of protrudent part was roughly 3.2 µm.

A question then arises: why are the erosion rate and machining quality of SD abrasive better than those of SiC abrasive? As mentioned before, green SiC abrasive particles driving by the low-pressure air jet cannot crush the harder SiC grains. Nevertheless, erosion has occurred,
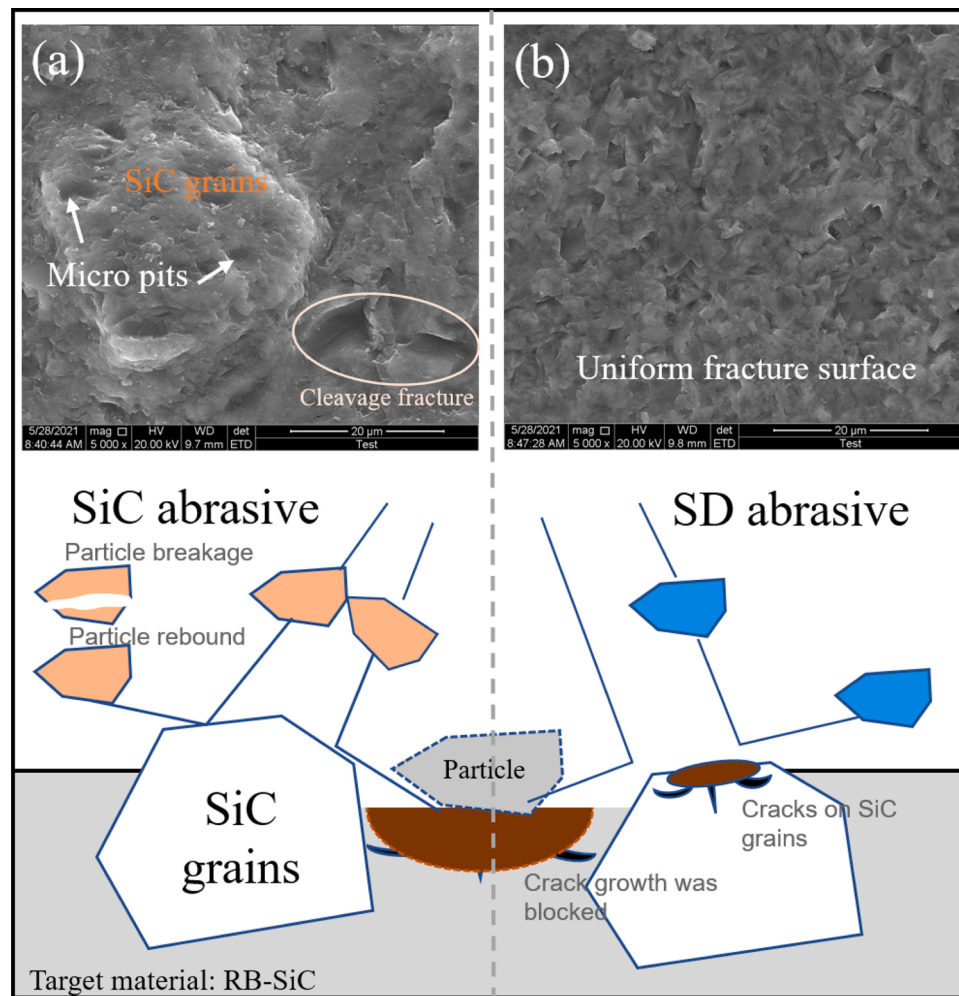
Fig. 8. SEM images and the related erosion mechanisms of RB-SiC surface eroded by (a) SiC abrasive and (b) SD abrasive.

forming an average erosion depth of about 11.3 μm (see Table 3), which is lower than the average dimension of SiC grains (about 30 μm as seen in Fig. 1). It is implied that in the machining of RB-SiC with SiC abrasive, only removal of Si matrix occurs in the process. As a result, the eroded surface of RB-SiC leaves numerous exposed SiC grains that cannot be removed, and micro-pits are generated around the grains due to the removal of Si phase. In this case, the surface characteristics indicate that shearing is dominant during particle erosion. The exposed SiC grains will be to some degree protective of the target, so the depth is shallow and it is difficult to deepen it further. It is found that the quality of the eroded surface mainly depends on the material structure, and the surface roughness is related to the amount and dimension of exposed SiC grains. Therefore, the machined surface presents a quite rough appearance covered with unbroken grains. Base on this information, the related erosion mechanism can be illustrated in Fig. 9(a). When the SD abrasive was employed, since its hardness is obviously higher than the hardness of SiC grains (see Table 1), the exposed SiC grains will be shattered by impact and removed from the substrate. As a result, the eroded surface exhibits a smooth morphology with a lower roughness and a deeper erosion depth in comparison with the eroded surface by SiC abrasive. The related erosion mechanism is illustrated in Fig. 9(b).

Based on the observations of damaged surfaces, the particle erosion mechanisms of RB-SiC using Al_2O_3, SiC and SD abrasive can be concluded in Fig. 10. The softest abrasive, Al_2O_3, has the insufficient hardness to machine. Most of the impacting abrasives cannot affect the SiC surface, and there is almost no damage on the surface of SiC grains. Only a small amount of Si matrix is removed, resulting in the

morphology shown in Fig. 10(a). While for SiC abrasive, all levels within the machined texture are lower than the raw surface, indicating that gradual fatigue damage may occur on the surface of SiC grains, as proved in Fig. 10(b). In this case, Si matrix is preferentially removed from the substrate compared to SiC grains. When SD abrasive is employed, the brittle erosion occurs for both Si and SiC phases. In this situation, due to the grain fragmentation, the entire surface is flat, and the machining depth (*h*) is deep, as shown in Fig. 10(c).

3.1.3. Crack-free texture

In the study of using dry AJM on RB-SiC, Huang et al. (2001) found that microcracks appeared on the erosion surface of Si matrix. The remaining micro-cracks on the surface may lead to premature failure of the components, which produces a serious problem when applied to micro-machining of brittle materials. However, in this study of using wet AJM, it is of interest to indicate that although the erosion of Si matrix takes place dominantly in brittle mode, no obvious signs of cracks were found on all the slurry erosion surfaces of RB-SiC (see Fig. 11). It should be noted that cracks are most likely to occur under the machining conditions with relatively large erosion energy. Therefore, the surfaces eroded under the conditions of a particle size of 13 μm and an air pressure of 0.6 MPa were observed here.

It is difficult to infer that there are no cracks on the subsurface of the material on the basis of current results, but it can be confirmed that there are no cracks on the eroded surface. The reason for forming the crack-free appearance may be related to the particle flow in the perpendicular impingement of jets.
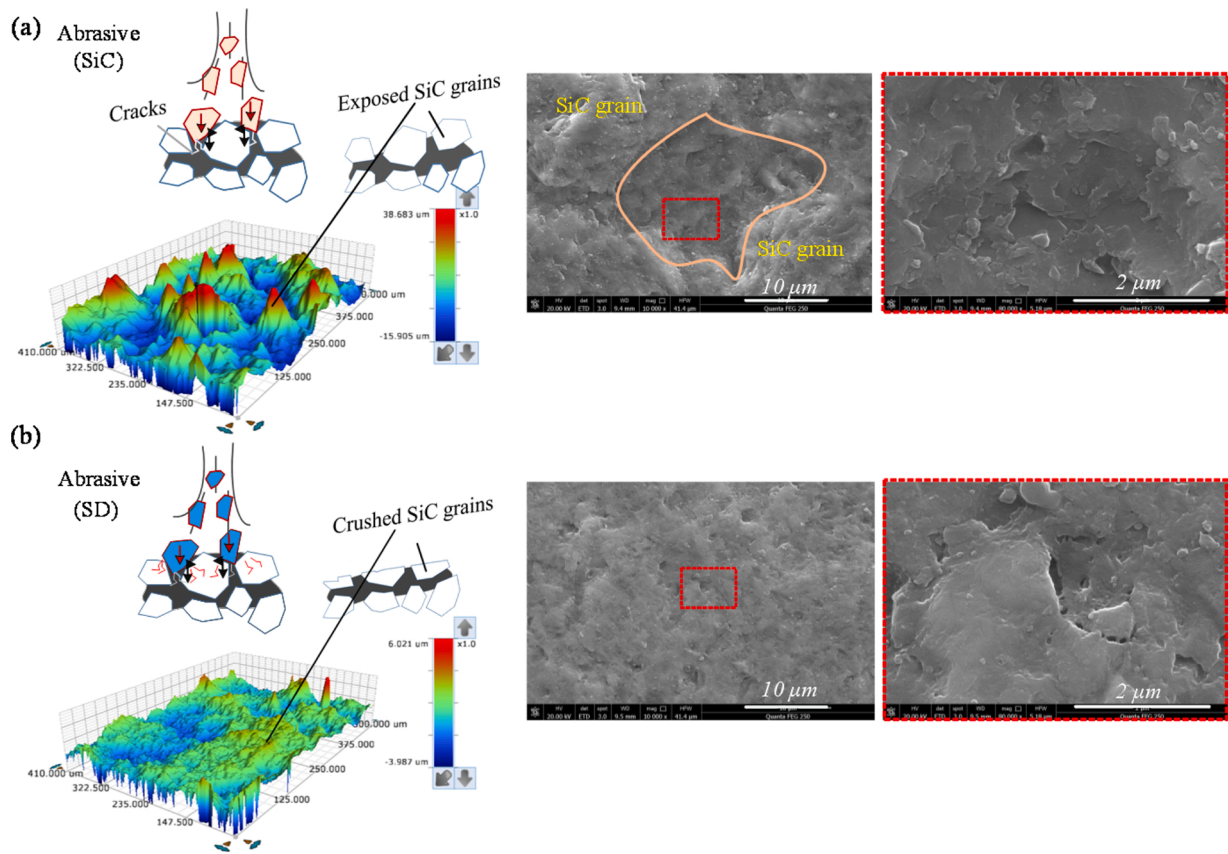
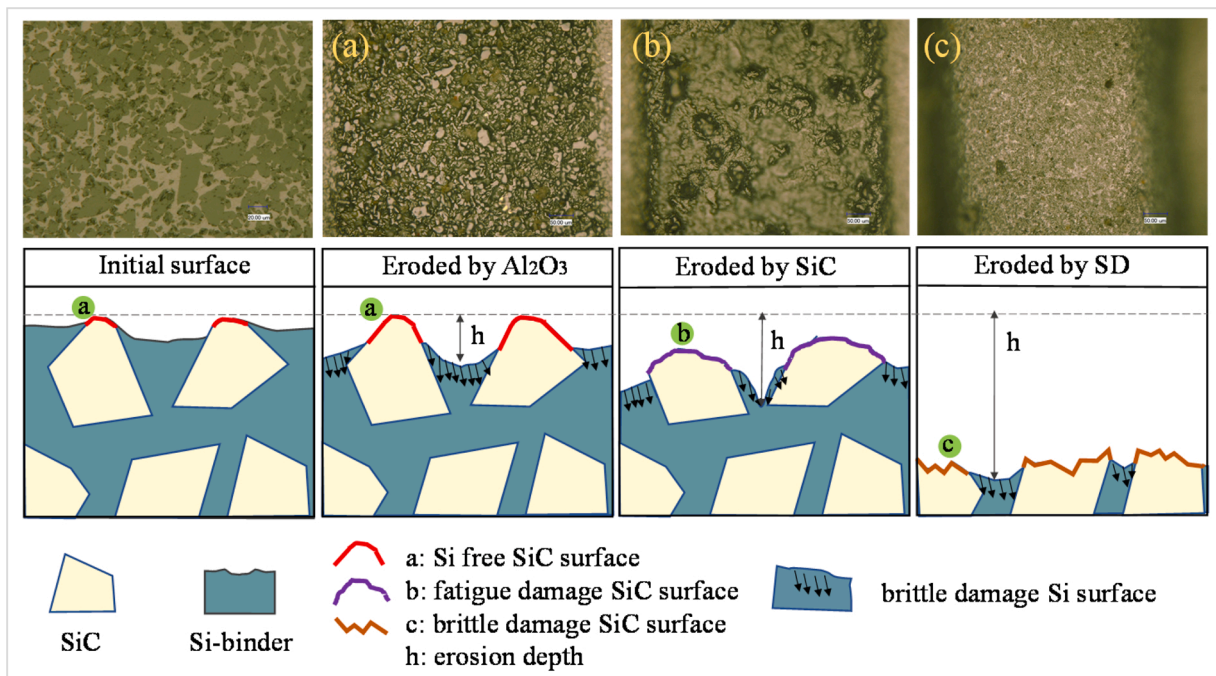**Fig. 9.** Mechanisms for the erosion by (a) SiC and (b) SD abrasive.

Fig. 10. Mechanisms of RB-SiC surface eroded by (a) Al₂O₃, (b) SiC and (c) SD abrasive.

To trace the particle trajectories, a series of simulations were performed using ANSYS Fluent 16.1 (ANSYS Inc., Cecil Township, PA, USA).The mixture model and DPM involved in the Fluent software were used to simulate the complex particle-laden flows under the dry and wet jet conditions. The standard *k-ε* turbulence model was employed to investigate the turbulent flow with high Reynolds number. In the 3D modeling, fluid flows into a cylindrical nozzle with length of 3 mm and inner diameter of 1.9 mm through a velocity inlet boundary of 100 m/s.
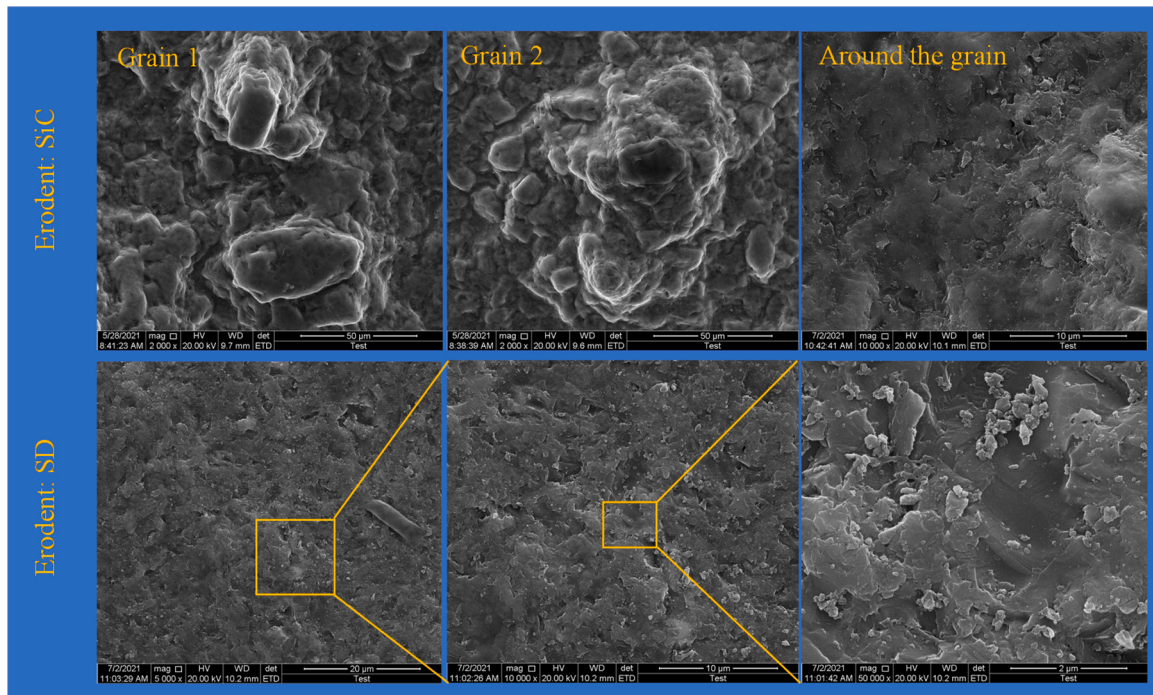
Fig. 11. Crack-free surfaces eroded by SiC and SD abrasives at particle size of 13 μm, air pressure of 0.6 MPa and feed distance of 20 μm.
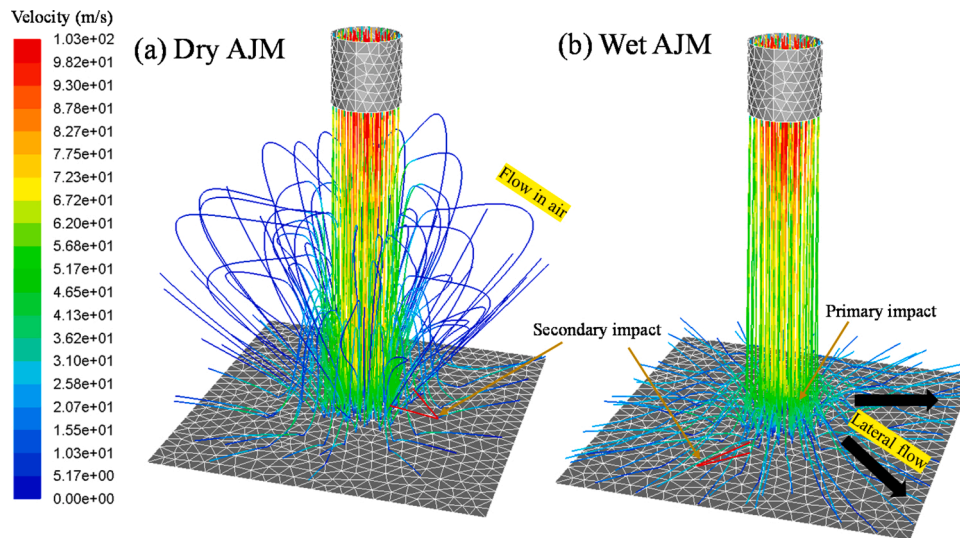

Fig. 12. Schematics of the particle flow in the perpendicular impingement of (a) dry and (b) wet AJM jet on a target plate.

The outer domain of the nozzle was set to be a cube with side length of 10 mm (viz. standoff distance). To simulate the air environment, jet flows out of the computational domain through a pressure outlet boundary of 101,1325 Pa. The inner surface of nozzle and target surface were treated as smooth no-slip walls. Half of the target surface was designed as a groove shape (2-mm regular triangular array), and the other half was designed as a plane with the aim of tracing the particle trajectories on the rough RB-SiC surface and the smooth Si surface, respectively. The fluid viscosity in the dry jet is equal to the air viscosity (20 °C, 17.894e-6 kg/(m·s)). The fluid viscosity in the wet jet was assumed to increase tenfold. Particle size of 13 μm and density of 3210 kg.m^{-3} were employed in the DPM. With these setting parameters, the simulation results are shown in Figs. 12–14.

As shown in Fig. 12(a), particles in the dry jet hit the surface almost perpendicularly. After the first impact, most of them are floating in the air. A few particles will hit the surface again with a relatively large impact angle. Brittle materials usually obtain the maximum erosion rate and produce the deepest radial cracks at these larger impact angles. Obviously, these vertically impacting particles are easy to directly contact with the Si matrix within the material to cause cracks. However, as sketched in Fig. 12(b), due to the large stagnation effect, most of the particles lose their impact energy. They are strongly deflected by the water flow and then hit the surface at an angle less than 90°. In this case, most of them slide towards the Si surface with a certain horizontal velocity instead of hitting vertically. With these low impact angles and low impact energy, the ability to induce cracks is greatly reduced. After the first impact, most of the particles will flow along the machined surface. The lateral flow has a sliding grinding effect that facilitates the formation of crack-free surfaces. Further, the sliding grinding effect can be improved by the micro vortex effect, as illustrated in Fig. 13. Due to the
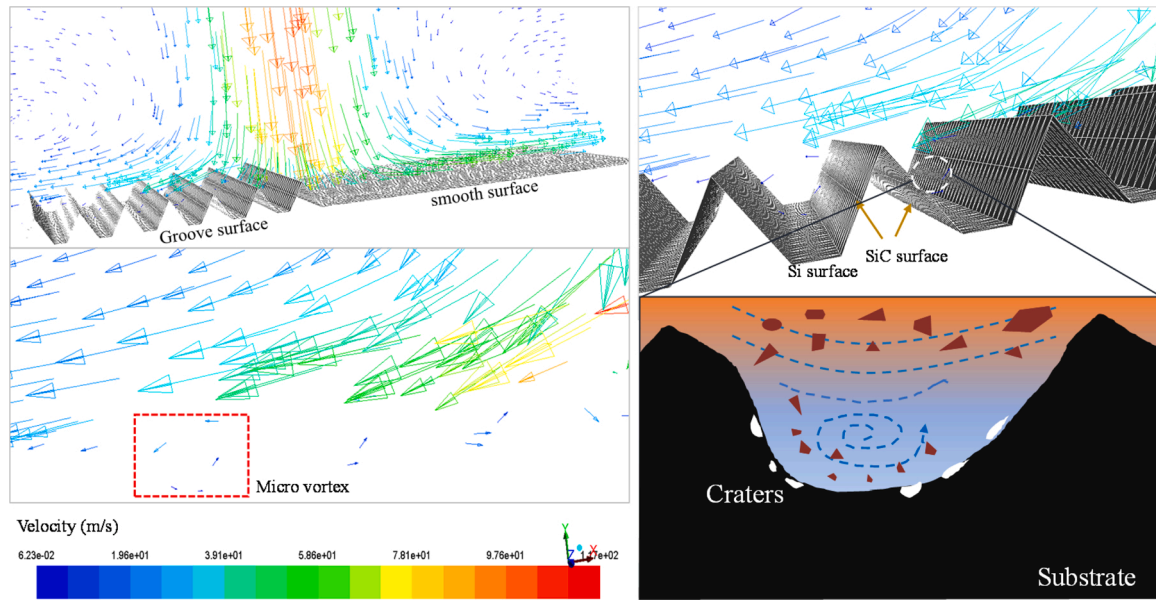
Fig. 13. Micro-vortex producing in the lateral flow during the wet jet erosion of RB-SiC.

presence of exposed SiC grains, the erosive surface exhibits a trench-like morphology. When the slurry flows through the rough surface at high speed, micro-vortexes will be formed between the two grains. Compared with the smooth surface, the velocity gradient in the gap will increase to a certain extent. At the same time, the flow direction of vortex will transform part of the frictional resistance into the driving force, as noted by Tang et al. (2017). In the narrow space between two adjacent SiC grains, the driving force allows the particles to roll and move freely. The motion of the rolling particles can smoothen the cracks on the newly cracked surface, thus resulting in the crack-free surface morphology shown in Fig. 11.

On the other hand, cracks have been found on the erosion surface of wet AJM of neat Si (see Fig. 6), whereas as mentioned before, no obvious signs of cracks were found on Si matrix surfaces within RB-SiC. The reason may be related to the presence of SiC grains, which can alter the particle impact trajectory. As shown in Fig. 14(a), when particles impact the smooth Si substrate, they will directly contact and then bounce. Obviously, these vertical impacts of particles can easily induce cracks on the brittle material. As shown in Fig. 14(b), when particles impact the RB-SiC substrate, due to the irregular surface, there are some secondary collisions, and the impact trajectories of particle are disrupted. A considerable number of particles will rebound or even break after hitting the SiC grains, and then lose their kinetic energy. After the first impacts, only a few particles slip to the Si surface at the bottom of the groove. The direction and angle of secondary impacts are chaotic. The speed of particles entering the groove structure is reduced, thus resulting in a reduction in the ability to generate cracks. In addition, even if the cracks occur, the presence of a tough secondary phase (SiC grains) can prevent the extension of cracks, therefore reducing the tendency for fracture (see Fig. 8). In other words, due to the protective effect of SiC grains, the Si matrix surface in the RB-SiC structure is more difficult to crack than the smooth Si surface.

In summary, dry jets are easy to induce cracks; although the wet (slurry) jets have the effect of grinding and polishing, cracks still exist on the surface of neat Si, indicating that the enhanced polishing effect caused by micro-vortexes plays an important role in the formation of crack-free surface during the machining of RB-SiC.

3.2. Method of obtaining a more accurate shape

For a surface texturing application, in addition to the analysis of

bottom surface, the texture profile also needs attention. In general, rectangular profile is desired because it can generate a stable hydrodynamic pressure. Although the S-type feed mode has been reported in many AJMs, the sidewall and bottom profile of the machined textures are related to the target material, as noted by Haghbin et al. (2018). Since the target material is RB-SiC, it is necessary to optimize the parameters to obtain a more precise machining profile. In this section, air pressure was fixed at 0.6 MPa, and a feed distance of 100 μm was used to ensure the flatness in the groove direction and obtain an acceptable machining time. The nozzle motion speed (V_X) was fixed at 1 mm/s, and its change had little effect on the machining results. Due to the excellent machining properties, SD abrasive was chosen to further optimize the machining profiles by adjusting other parameters, including the mask thickness (0.2–3 mm), nozzle motion speed (V_Y) (0.1–0.5 mm/s) and particle size (6.5–13 μm). These adjustable ranges were determined by the experimental tests.

It is found that under the different combination parameters, the machined textures present some variations both in profile and sidewall slope. Within the range of their variations, three kinds of bottom profiles were obtained, as seen in Fig. 15(a–c). The bottoms can be divided into almost flat, concave (U-shape) and convex (W-shape). The flat bottom was obtained under the operating conditions of 0.2-mm mask thickness, 0.4-mm/s nozzle motion speed (V_Y) and 13-μm average particle size. This shape is similar to an inverted cone platform, and the size of the cone top is larger than that of the cone bottom. The concave bottom was fabricated at the conditions of 3-mm mask thickness, 0.3-mm/s nozzle motion speed (V_Y) and 13-μm particle size. This contour is like the inside profile of a bowl. Under the conditions of 1-mm mask thickness, 0.4-mm/s nozzle motion speed (V_Y) and 8-μm average particle size, the sidewalls of the machined texture are relatively steep, and the bottom presents a convex shape where exists a central region with a smaller depth and edges with a deeper depth.

Obviously, the evolution of machining profile is related to the change of operating parameters. As illustrated in Fig. 16, the texture sidewall may depend on the balance between the excess erosion (also called under-etching) and insufficient erosion. Excess erosion is the excessive machining of sidewall under the mask, which is a common phenomenon in masked jet machining, as investigated by Haghbin et al. (2018). It is associate with the secondary impact in which particle bounces from the bottom surface. Insufficient erosion is the insufficient machining of sidewall, and there is a large erosion depth near the mask edge, which is
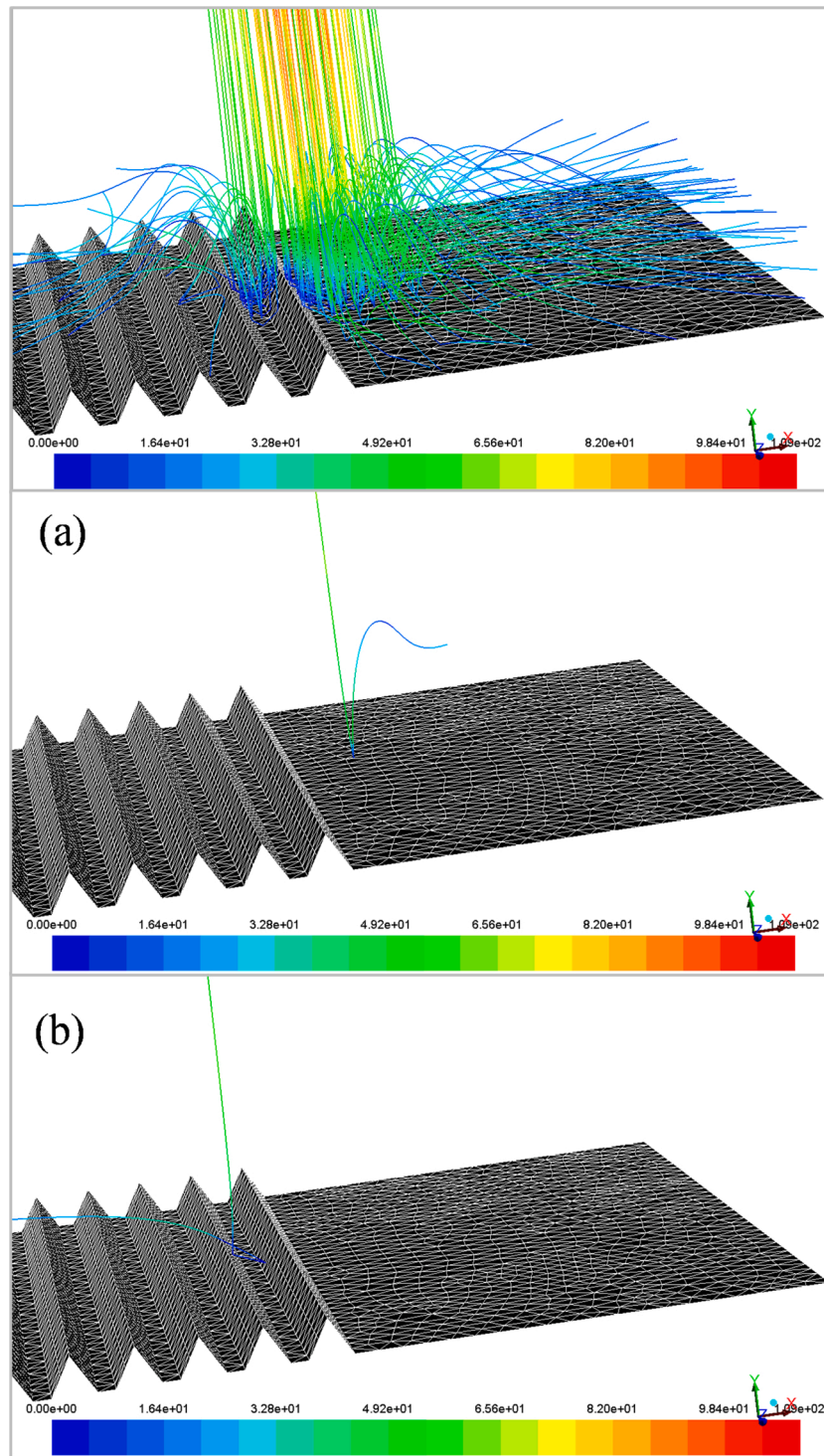
Fig. 14. The trajectory of particle hitting (a) the plane and (b) the groove.

associated with the impact by particles rebounding from mask edge. Both excess erosion and insufficient erosion are the undesired machining results and should be avoided.

How to control the balance between the excess erosion and insufficient erosion is a key to improve the transfer accuracy of masked jet machining and ensure the flatness of bottom. Obviously, the mask thickness, nozzle motion speed (V_Y) and particle size are of significant influence on particle reflection, thus inevitably affecting the machining profile. Therefore, experiments were conducted to explore the effect of these parameters on the machining profile.

3.2.1. Effect of mask thickness

To investigate the intensity of particles rebounding from the mask wall, experiments were conducted with the mask thickness decreased from 3 mm to 1 mm and then 0.2 mm. Other experimental conditions are the average particle size of 8 μm and nozzle motion speed (V_Y) of 0.5 mm/s. Fig. 17 presents the cross-sections of channels machined at the three masks. Masks with thickness of 1 and 3 mm create a deep depth near the mask edge, especially in the case of using 1-mm thickness. This may be due to the fact that in the case of using thick masks, the particles rebounding from the mask wall are concentrated near the mask edge,
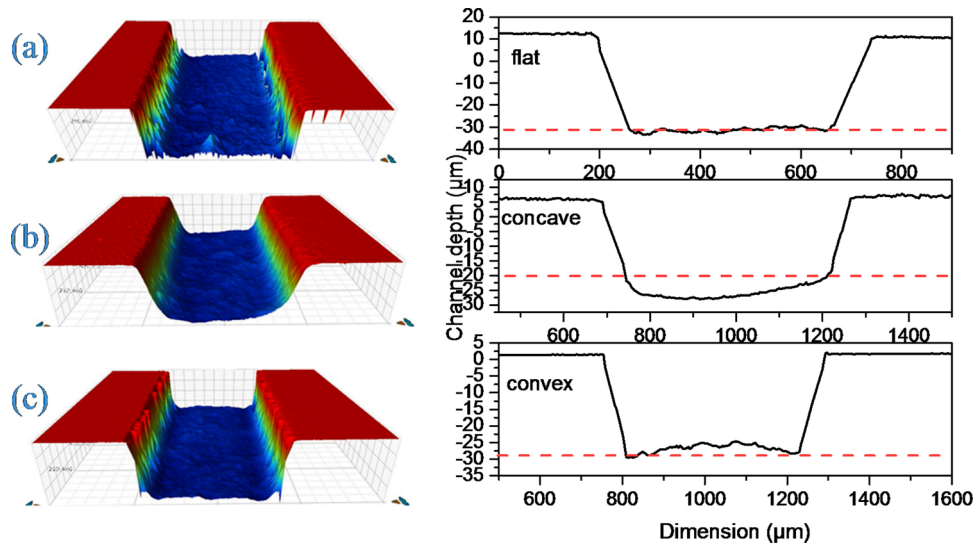
Fig. 15. Three kinds of channels machined by wet AJM with SD abrasive particles: (a) flat, (b) concave, and (c) convex.
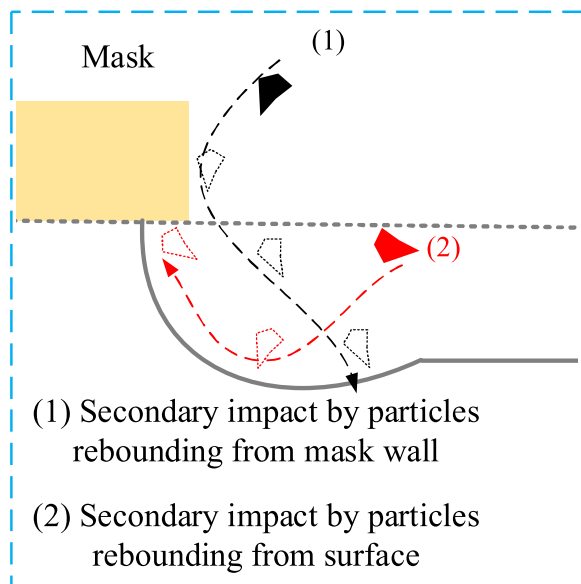

Fig. 16. Schematic diagram of texture formation due to two kinds of particle impacts (Ghobeity et al., 2009).

Fig. 17. Cross-sectional profiles of textures machined on RB-SiC as a function of mask thickness.

causing a relatively large erosion depth there, as illustrated in Fig. 18. When using the mask with a 3-mm thickness, the particles bounce too violently. Most particles bounce to further places and lose their impact kinetic energy, so the edge depth of using 3-mm mask is lower that of using the 1-mm mask. Obviously, as the mask thickness decreases, the number of particles rebounding from the mask wall surface reduces, so a flat bottom was obtained in the machining using 0.2-mm mask. Thick mask allows the particles to strike a position away from the mask edge, thus the sidewall exhibits an insufficient erosion. In the processing with a thin mask, particles can reach the bottom, which increases the number of particles rebounding from the bottom surface, causing the sidewalls to exhibit excessive erosion. Therefore, in order to obtain a flat bottom, it is recommended to use a relatively thin mask.

3.2.2. Effect of nozzle motion speed

Fig. 19 presents the influence of nozzle motion speed (V_Y) on texture profile under the conditions of mask thickness of 0.2 mm and average particle size of 8 μm. It can be seen that a deeper machining depth is

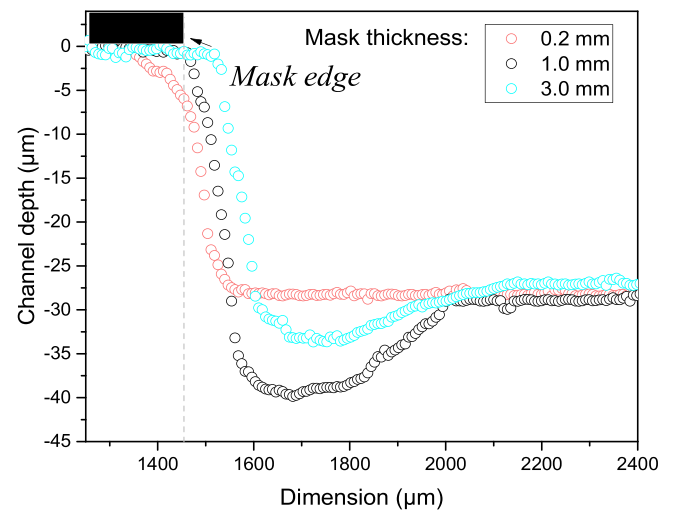obtained at a smaller nozzle motion speed (V_Y), and the depth near the mask edge is slightly bigger than that of center. While a flat bottom is obtained in the processing with a relatively large nozzle motion speed (V_Y). With the decrease of nozzle motion speed (V_Y), the excess erosion of sidewall is increasingly significant. Small nozzle motion speed (V_Y) allows more residence time near the mask edge. It is clear that the deep depth near the mask edge and the excess erosion of sidewall are related to the aggravation of particle rebound caused by excessive residence time. To avoid the deep depth near the mask edge, a relatively big nozzle motion speed (V_Y) should be chosen.

3.2.3. Effect of particle size

Fig. 20 exhibits the influence of particle size on the texture profile under the optimized conditions of mask thickness of 0.2 mm and nozzle motion speed (V_Y) of 0.5 mm/s. As shown in Fig. 20, the particle size has a significant effect on the texture profile. The larger particle size yields a deeper depth and a coarser surface than the small one. Small particles tend to flow close to the mask edge and get into the gap between the mask and the workpiece, thus resulting in excess erosion of sidewall. Large particles with enough impact kinetic energy tend to bounce away from the mask edge, so the sidewall exhibits an insufficient erosion,
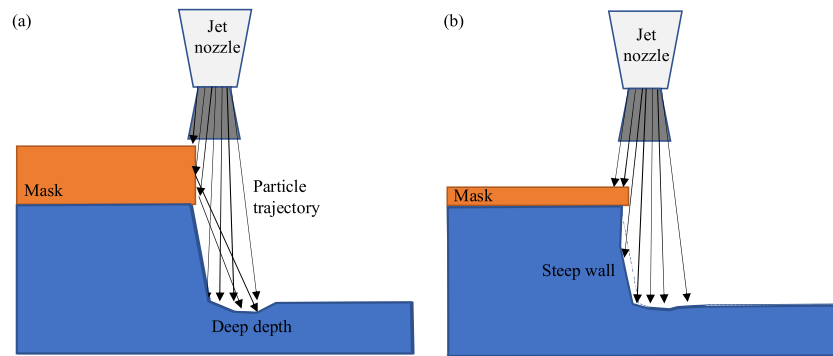
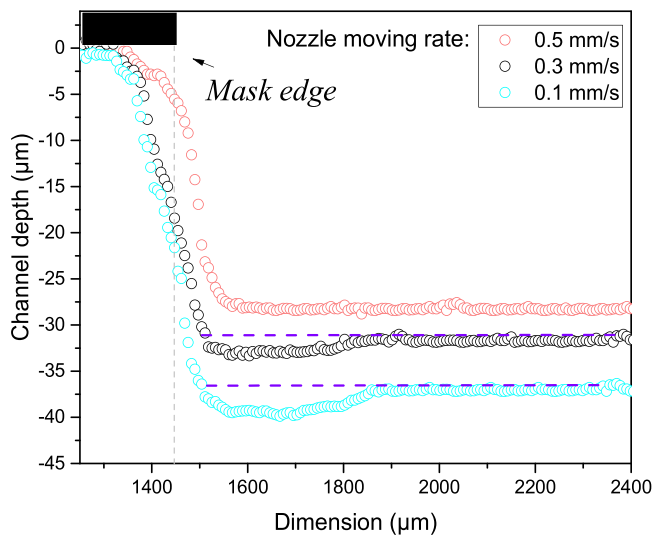**Fig. 18.** Schematic of particle deflection for (a) thick and (b) thin mask.

Fig. 19. Cross-sectional profiles of textures machined on RB-SiC as a function of nozzle moving rate.
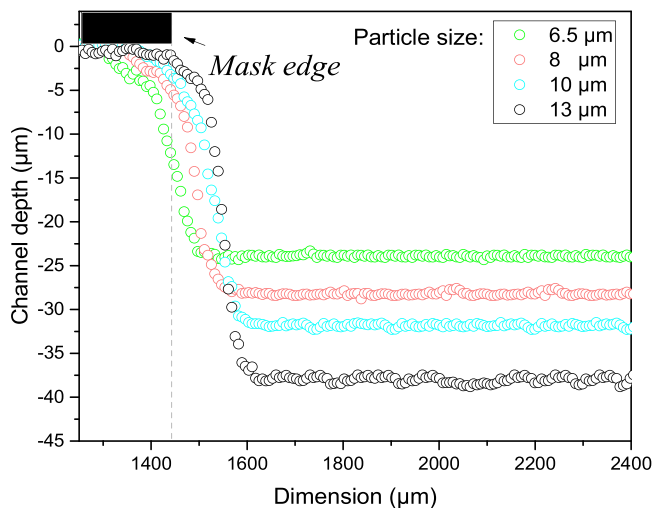

Fig. 20. Cross-sectional profiles of textures machined on RB-SiC as a function of particle size.

especially in the machining with 13-μm average particle size. Therefore, with the optimized parameters of 0.2-mm mask thickness and 0.5-mm/s nozzle motion speed (V_Y), the average particle size of 8 μm should be preferred. Sizes larger than 8 μm can be used to avoid the excess erosion

if need.

3.2.4. Application of surface texturing

As seen from the previous sections, a mask thickness of 0.2 mm, a nozzle motion speed (V_Y) of 0.5 mm/s and the SD abrasive with a particle size of 8 μm should be chosen preferentially. Under these machining parameters, the linear and curved grooves were fabricated to demonstrate the capability of the wet AJM on RB-SiC. Fig. 21 shows the machined linear groove has a flat bottom, including the transverse and longitudinal sections. The machined feature presents a well-defined boundary and there is no waviness in the bottom. Fig. 22 shows an array of spiral grooves that manufactured on a rotor ring surface, indicating that the wet AJM process has the potential application of fabricating complex micro textured topographies on RB-SiC surface used for mechanical seals.

4. Level of the obtained surface roughness

In general, the stress response of a single-phase material is evenly distributed on its structure, so the resulting grooves are continuous and uniform. In comparison, it is more difficult to obtain a low-roughness surface on a non-uniform material like RB-SiC. Fortunately, the low-roughness surface was achieved by the optimized wet AJM process. To prove this low level of roughness, the comparison between the roughness of RB-SiC in the present work and glass in the published work related to abrasive jet polishing is given in Fig. 23. It can be found that the two-phase RB-SiC can be machined to have the same grade of roughness as the single-phase glass, sometimes even lower than the value of dry AJM of glass. To the knowledge of the authors, surface texture with such low roughness is difficult to be obtained on RB-SiC in conventional machining conditions.

Fig. 24 compares the surface roughness (R_a) in RB-SiC machined by the wet AJM in this paper, abrasive slurry jet in the work of Nguyen et al. (2018), diamond disk polishing in the work of Nguyen et al. (2018) and micro-grinding in the works of Zhang et al. (2020) and Zhang et al. (2015). From Fig. 23, it can be found that the surface roughness in RB-SiC machined by wet AJM is relatively low, even comparable to the surface roughness by diamond disc polishing. It should be noted that in the case of using diamond disk polishing and micro-grinding, the low roughness is achieved by the ductile removal mode with low material removal rate, thus the roughness is reduced at the expense of processing time. In addition, these contact methods are mainly used for polishing-based surface finishing and are not flexible for the machining of three-dimensional microfeatures.

5. Conclusions

In the present study, a wet abrasive jet machining (wet AJM) process was successfully optimized to fabricate rectangular textures with smooth and flat bottom on a two-phase material, RB-SiC. The new
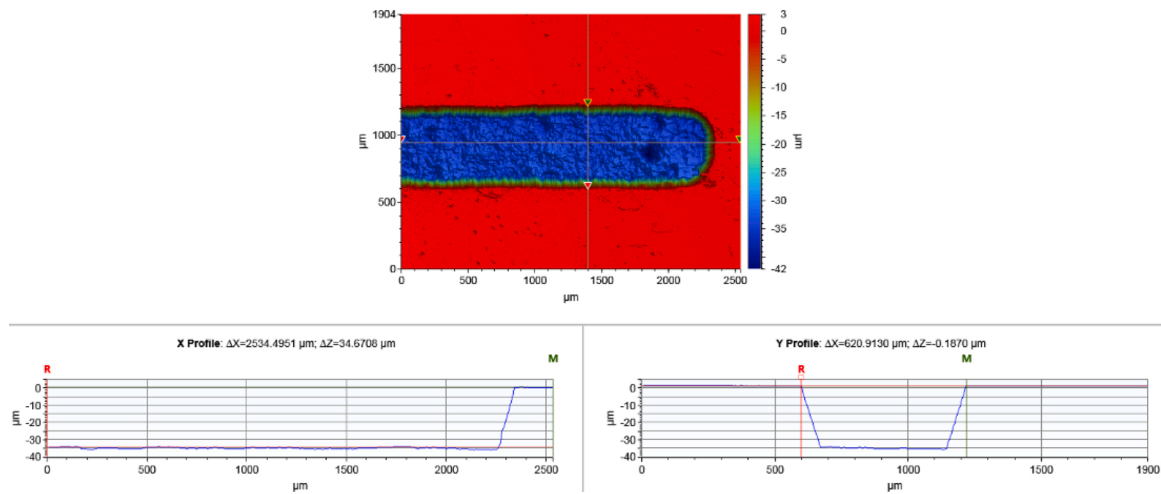
Fig. 21. Cross-sectional profiles of channel machined by wet AJM with the optimized parameters (i.e., RB-SiC ring).
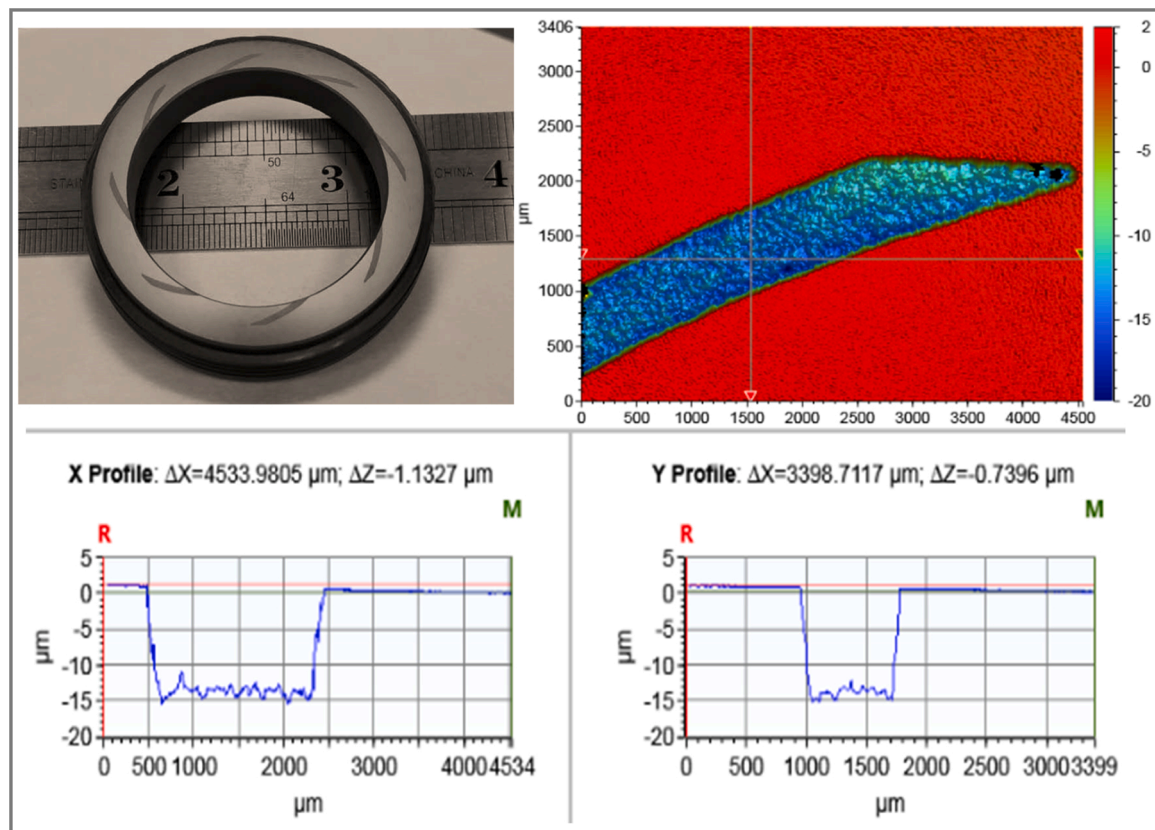

**Fig. 22.** Surface texturing on the mechanical seal rotor ring (i.e., RB-SiC ring).

findings are concluded as follows:

(1) In the wet AJM of RB-SiC, the increase of impact energy (related to air pressure and particle size) and machining time (related to feed speed and feed distance) was found to have a significant effect on the machining efficiency, but have no or little effect on the roughness.

(2) Hardness of the employed abrasive is the most important factors determining both machining efficiency and roughness. The softest abrasive, Al_2O_3, has the insufficient hardness to machine. Using the hardest SD abrasive, not only significantly improves the machining efficiency, but also reduces the surface roughness.

Under certain parameters, machining efficiency of SD can be 20.93 and 4.37 times that of Al_2O_3 and SiC, respectively. Additionally, a relatively low roughness can be obtained by SD abrasive (0.6 μm vs 2.6 μm using SiC abrasive). SD abrasive can be therefore recommended for jet machining of composites containing hard and brittle reinforcements.

(3) For SiC abrasive, erosion appears to occur mainly by shearing and wedging action to preferentially remove the Si binder, and then SiC grains are exposed on the surface. In this case, RB-SiC surface is subjected to a mixture of brittle erosion of Si phase and low-cycle fatigue of SiC phase. While for SD abrasive, erosion may
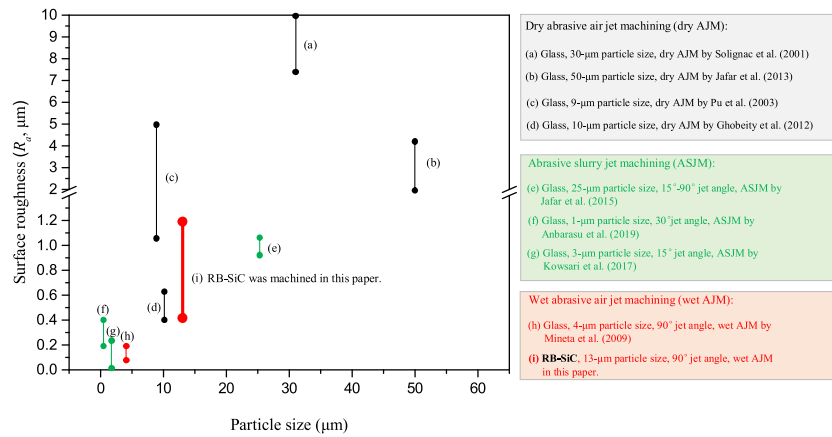
Fig. 23. Comparison of surface roughness between glass material machined by different abrasive jet polishing processes and RB-SiC material machined by wet AJM in this paper. References include Solignac et al. (Solignac et al., 2001), Jafar et al. (Jafar et al., 2013), Pu et al. (Pu et al., 2003), Ghobeity et al. (Ghobeity et al., 2012), Jafar et al. (Jafar et al., 2015), Anbarasu et al. (Anbarasu et al., 2019), Kowsari et al. (Kowsari et al., 2017) and Mineta et al. (Mineta et al., 2009).
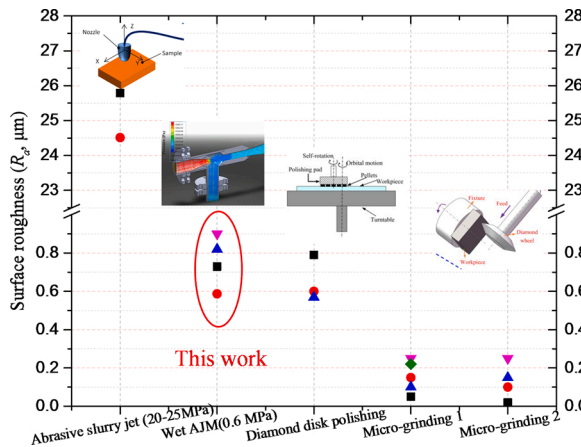
Fig. 24. Comparison of surface roughness in RB-SiC machined by various methods.

include grain splintering. In this case, the surface is mainly subjected to a brittle erosion mechanism.

(4) Although there was a brittle erosion mode during the processing, no obvious cracks were found on the eroded surface. The water is found to play a great role in forming the surface without mechanical cracking damage. Especially in the narrow space between two adjacent SiC grains, driving force allows the particles to roll and move in a certain direction, which can smoothen the cracks on the newly cracked surface.

Although only one brittle-matrix composite was studied, it is likely that many of the conclusions hold for other metal or polymer matrix composite materials and ceramic reinforcement materials. No matter which type of jet machining is used, the hardness of the employed abrasive should be high enough relative to the hardness of the target during the machining of hard ceramic materials. Base on this information, the high hardness of SD abrasive is of interest from an empirical aspect. The sliding grinding effect brought by water can also be applicable to other water-based jets, such as abrasive slurry jets and abrasive water jets. In terms of application, this paper not only open a new approach to efficiently introduce desired micro-patterns on ceramic surface used for mechanical seals, but also provide the basis to understand the particle erosion mechanism during the dry and wet AJM of two-phase material. However, because of the divergence of jet, wear-resistant mask with finer openings will need to be developed to obtain

sub-micro patterns. In addition, the effect of fine opening and the interaction among operating parameters should be investigated.

Author agreement

All the authors have seen and approved the final version of the manuscript being submitted. This is an original paper which has neither previously, nor simultaneously, in whole or in part been previously published. The article has not been submitted to peer review, nor is in the process of peer reviewing, nor has been accepted for publishing in another journal.

Declaration of Competing Interes

The authors declare that they have no known competing financial interests or personal relationships that could have appeared to influence the work reported in this paper.

Acknowledgments

References

Anbarasu, K.G., Vijayaraghavan, L., Arunachalam, N., 2019. Effect of multi stage abrasive slurry jet polishing on surface generation in glass. J. Mater. Process. Technol. 267, 384–392.

Belloy, E., Sayah, A., Gijs, M.A.M., 2002. Micromachining of glass inertial sensors. J. Microelectromech. Syst. 11 (1), 85–90.

Chen, C.Y., Chung, C.J., Wu, B.H., Li, W.L., Chien, C.W., Wu, P.H., et al., 2012. Microstructure and lubricating property of ultra-fast laser pulse textured silicon carbide seals. Appl. Phys. A Mater. Sci. Process. 107 (2), 345–350.

Clijsters, S., Liu, K., Reynaerts, D., Lauwers, B., 2010. EDM technology and strategy development for the manufacturing of complex parts in SiSiC. J. Mater. Process. Technol. 210 (4), 631–641.

Ghobeity, A., Crabtree, H.J., Papini, M., Spelt, J.K., 2012. Characterisation and comparison of microfluidic chips formed using abrasive jet micromachining and wet etching. J. Micromech. Microeng. 22 (2), 025014.

Ghobeity, A., Papini, M., Spelt, J.K., 2009. Abrasive jet micro-machining of planar areas and transitional slopes in glass using target oscillation. J. Mater. Process. Technol. 209 (11), 5123–5132.

Haghbin, N., Ahmadzadeh, F., Papini, M., 2018. Masked micro-channel machining in aluminum alloy and borosilicate glass using abrasive water jet micro-machining. J. Manuf. Process. 35, 307–316.

Huang, Z., Li, Z.Z., Yuan, X., 2001. The effect of reinforcing particles on the erosive wear behavior of particles reinforced silicone matrix composite coating. Wear 249 (12), 1046–1050.

Ishikawa, Y., Yao, Y.Z., Sugawara, Y., Sato, K., Sekiguchi, T., 2014. Comparison of slicing-induced damage in hexagonal SiC by wire sawing with loose abrasive, wire

sawing with fixed abrasive, and electric discharge machining. J. Appl. Phys. 53, 071301.

Iwai, Y., Matsubara, T., Hirai, Y., Hogmark, S., 2009. Development of a new type micro slurry-jet erosion (MSE) tester for evaluation of wear properties of hard thin coatings. Lubr. Sci. 21 (6), 213–226.

Jafar, R.H., Papini, M., Spelt, J.K., 2013. Simulation of erosive smoothing in the abrasive jet micro-machining of glass. J. Mater. Process. Technol. 213, 2254–2261.

Jafar, R.H., Nouraei, H., Emamifara, M., Papini, M., Spelt, J.K., 2015. Erosion modeling in abrasive slurry jet micro-machining of brittle materials. J. Mater. Process. Technol. 17, 127–140.

Kowsari, K., Schwartzentruber, J., Papini, M., Spelt, J.K., 2017. Erosive smoothing of abrasive slurry-jet micro-machined channels in glass, PMMA, and sintered ceramics: Experiments and roughness model. Precis. Eng. 49, 332–343.

Manoj, M., Jinu, G.R., Muthuramalingam, T., 2018. Multi response optimization of AWJM process parameters on machining TiB2 particles reinforced Al7075 composite using Taguchi-DEAR methodology. Silicon 10, 2287–2293.

Melentiev, R., Fang, F.Z., 2020. Tailoring of surface topography for tribological purposes by controlled solid particle impacts. Wear 444-445, 203164.

Mineta, T., Takada, T., Makino, E., Kawashima, T., Shibata, T., 2009. A wet abrasive blasting process for smooth micromachining of glass by ductile-mode removal. J. Micromech. Microeng. 19, 015031.

Nguyen, T., Liu, D., Thongkaew, K., Li, H., Qi, H., Wang, J., 2018. The wear mechanisms of reaction bonded silicon carbide under abrasive polishing and slurry jet impact conditions. Wear 410-411, 156–164.

Nouraei, H., Wodoslawsky, A., Papini, M., Spelt, J.K., 2013. Characteristics of abrasive slurry jet micro-machining: a comparison with abrasive air jet micro-machining. J. Mater. Process. Technol. 213 (10), 1711–1724.

Park, D.S., Seo, T.I., Cho, M.W., 2005. Mechanical etching of micro pockets by powder blasting. Int. J. Adv. Manuf. Technol. 25 (11), 1098–1104.

Patten, J., Gao, W., Yasuto, K., 2005. Ductile Regime Nanomachining of Single-Crystal Silicon Carbide. J. Manuf. Sci. Eng. 127 (3), 522–532.

Pu, Q., Luttge, R., Gardeniers, H., van den Berg, A., 2003. Comparison of capillary zone electrophoresis performance of powder-blasted and hydrogen fluoride-etched microchannels in glass. Electrophoresis 24, 162–171.

Rao, Xiaoshuang, Zhang, Feihu, Lu, Yanjun, Luo, Xichun, Chen, Fumin, 2020. Surface and subsurface damage of reaction-bonded silicon carbide induced by electrical discharge diamond grinding. Int. J. Mach. Tools Manuf. 154, 103564.

Saragih, A.S., Ko, T.J., 2009a. Fabrication of passive glass micromixer with third-dimensional feature by employing SU8 mask on micro-abrasive jet machining. Int. J. Adv. Manuf. Technol. 42 (5–6), 474–481.

Saragih, A.S., Ko, T.J., 2009b. A thick SU-8 mask for microabrasive jet machining on glass. Int. J. Adv. Manuf. Technol. 41 (7–8), 734–740.

Shen, X., Tu, Q., Deng, H., Jiang, G., Yamamura, K., 2015. Mechanism analysis on finishing of reaction-sintered silicon carbide by combination of water vapor plasma oxidation and ceria slurry polishing. Opt. Eng. 54 (5), 055106.

Solignac, D., Sayah, A., Constantin, S., Freitag, R., Gijs, M., 2001. Powder blasting for the realisation of microchips for bio-analytic applications. Sens. Actuators A Phys. 92, 388–393.

Tang, L., Zeng, Z., Wang, G., Liu, E., Li, L., Xue, Q., 2017. Investigation on superhydrophilic surface with porous structure: Drag reduction or drag increasing. Surf. Coat. Technol. 317, 54–63.

Wakuda, M., Yamauchi, Y., Kanzaki, S., 2002. Effect of workpiece properties on machinability in abrasive jet machining of ceramic materials. Precis. Eng. 26 (2), 193–198.

Wakuda, M., Yamauchi, Y., Kanzaki, S., 2003. Material response to particle impact during abrasive jet machining of alumina ceramics. J. Mater. Process. Tech. 132 (1), 177–183.

Yamamura, K., Yamamoto, Y., Deng, H., 2012. Preliminary study on chemical figuring and finishing of sintered SiC substrate using atmospheric pressure plasma. Procedia CIRP 3, 335–339.

Zhang, Quanli, To, Suelt, Zhao, Qingliang, Guo, Bing, 2015. Amorphization and C segregation based surface generation of Reaction-Bonded SiC/Si composites under micro-grinding. Int. J. Mach. Tools Manuf. 95, 78–81.

Zhang, Junjie, Han, La, Zhang, Jianguo, Liu, Haiying, Yan, Yongda, Sun, Tao, 2019. Brittle-to-ductile transition in elliptical vibration-assisted diamond cutting of reaction-bonded silicon carbide. J. Manuf. Process. 45, 670–681.

Zhang, Zhenzhong, Yao, Peng, Wang, Jun, Huang, Chuanzhen, Zhu, Hongtao, Liu, Hanlian, Zou, Bin, 2020. Nanomechanical characterization of RB-SiC ceramics based on nanoindentation and modelling of the ground surface roughness. Ceram. Int. 46, 6243–6253.